

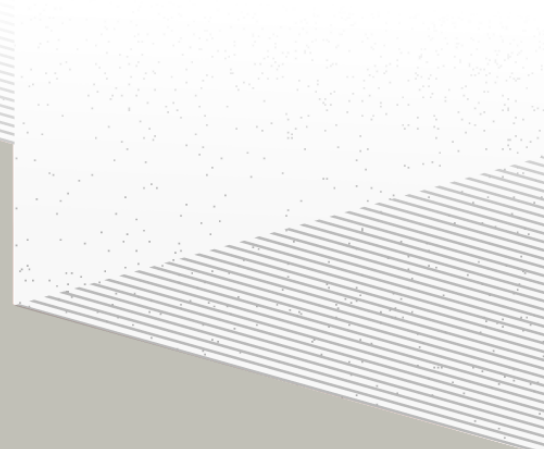
1

2

# THÈSE DE DOCTORAT DE

L'UNIVERSITÉ DE NANTES

ÉCOLE DOCTORALE N°596  
*Matière, Molécules, Matériaux*  
Spécialité : *Physique des particules*



Par

**Léonard Imbert**

**Precision measurement of solar neutrino oscillation parameters  
with the JUNO small PMTs system and test of the unitarity of the  
PMNS matrix**

Thèse présentée et soutenue à Nantes, le Too soon and too early at the same time  
Unité de recherche : Laboratoire SUBATECH, UMR 6457

## Rapporteurs avant soutenance :

Someone	Very high position, Somewhere
Someone else	Another high position, Somewhere else

## Composition du Jury :

Président :	Jacques Chirac	French president, France
Examinateurs :	Yoda	Master, Dagobha
Dir. de thèse :	Frédéric Yermia	Professeur, Université de Nantes
Co-dir. de thèse :	Benoit Viaud	Chargé de recherche, CNRS

## Invité(s) :

Victor Lebrin Docteur, CNRS/SUBATECH



## <sup>3</sup> List of Abbreviations

<b>ACU</b>	Automatic Calibration Unit
<b>BDT</b>	Boosted Decision Tree
<b>CD</b>	Central Detector
<b>CLS</b>	Cable Loop System
<b>CNN</b>	Convolutional NN
<b>DNN</b>	Deep NN
<b>GNN</b>	Graph NN
<b>GT</b>	Guiding Tube
<b>IBD</b>	Inverse Beta Decay
<b>IO</b>	Inverse Ordering
<b>JUNO</b>	Jiangmen Underground Neutrino Observatory
<b>LPMT</b>	Large PMT
<b>LS</b>	Liquid Scintillator
<b>MC</b>	Monte Carlo simulation
<b>ML</b>	Machine Learning
<b>NMO</b>	Neutrino Mass Ordering
<b>NN</b>	Neural Network
<b>NO</b>	Normal Ordering
<b>OSIRIS</b>	Online Scintillator Internal Radioactivity Investigation System
<b>PE</b>	Photo Electron
<b>PMT</b>	Photo-Multipliers Tubes
<b>ROV</b>	Remotely Operated under-LS Vehicle
<b>SPMT</b>	Small PMT
<b>TAO</b>	Taishan Antineutrino Observatory
<b>TR Area</b>	Total Reflexion Area
<b>TTS</b>	Time Transit Spread
<b>TT</b>	Top Tracker
<b>WCD</b>	Water Cherenkov Detector



# 4 Contents

5	<b>Contents</b>	1
6	<b>Remerciements</b>	3
7	<b>Introduction</b>	5
8	<b>1 Neutrino physics</b>	7
9	1.1 Standard model . . . . .	7
10	1.1.1 Limits of the standard model . . . . .	7
11	1.2 Historic of the neutrino . . . . .	7
12	1.3 Oscillation . . . . .	7
13	1.3.1 Phenomologies . . . . .	7
14	1.4 Open questions . . . . .	7
15	<b>2 The JUNO experiment</b>	9
16	2.1 Neutrinos physics in JUNO . . . . .	9
17	2.1.1 Reactor neutrino oscillation for NMO and precise measurements . . . . .	10
18	2.1.2 Other physics . . . . .	13
19	2.2 The JUNO detector . . . . .	14
20	2.2.1 Detection principle . . . . .	14
21	2.2.2 Central Detector (CD) . . . . .	16
22	2.2.3 Veto detector . . . . .	18
23	2.3 Calibration strategy . . . . .	19
24	2.3.1 Energy scale calibration . . . . .	19
25	2.3.2 Calibration system . . . . .	20
26	2.4 Satellite detectors . . . . .	20
27	2.4.1 TAO . . . . .	21
28	2.4.2 OSIRIS . . . . .	22
29	2.5 Software . . . . .	22
30	2.6 State of the art of the Offline IBD reconstruction in JUNO . . . . .	23
31	2.6.1 Interaction vertex reconstruction . . . . .	23
32	2.6.2 Energy reconstruction . . . . .	27
33	2.6.3 Machine learning for reconstruction . . . . .	29
34	2.7 JUNO sensitivity to NMO and precise measurements . . . . .	32
35	2.7.1 Theoretical spectrum . . . . .	33
36	2.7.2 Fitting procedure . . . . .	33

---

37	2.7.3 Physics results . . . . .	33
38	<b>3 Machine learning and Artificial Neural Network</b>	<b>35</b>
39	3.1 History of the Machine learning . . . . .	35
40	3.2 Boosted Decision Tree (BDT) . . . . .	35
41	3.3 Artificial Neural Network (NN) . . . . .	35
42	3.3.1 Fully Connected Deep Neural Network (FCDNN) . . . . .	35
43	3.3.2 Convolutional Neural Network (CNN) . . . . .	35
44	3.3.3 Graph Neural Network (GNN) . . . . .	35
45	3.3.4 Adversarial Neural Network (ANN) . . . . .	35
46	<b>4 Image recognition for IBD reconstruction with the SPMT system</b>	<b>37</b>
47	<b>5 Graph representation of JUNO for IBD reconstruction with the LPMT system</b>	<b>39</b>
48	<b>6 Reliability of machine learning methods</b>	<b>41</b>
49	<b>7 Discrimination of e+/e- events in JUNO</b>	<b>43</b>
50	<b>8 Joint fit between the SPMT and LPMT spectra</b>	<b>45</b>
51	<b>9 Conclusion</b>	<b>47</b>
52	<b>Bibliography</b>	<b>49</b>

<sup>53</sup> Remerciements



# 54 Introduction



<sup>55</sup> **Chapter 1**

<sup>56</sup> **Neutrino physics**

<sup>57</sup>

*The neutrino, or  $\nu$  for the close friends, a fascinating and invisible particle. Some will say that dark matter also have those property but at least we are pretty confident that neutrinos exists.*

<sup>58</sup> **1.1 Standard model**

<sup>59</sup> **1.1.1 Limits of the standard model**

<sup>60</sup> **1.2 Historic of the neutrino**

<sup>61</sup> **First theories**

<sup>62</sup> **Discovery**

<sup>63</sup> **Milestones and anomalies**

<sup>64</sup> **1.3 Oscillation**

<sup>65</sup> **1.3.1 Phenomologies**

<sup>66</sup> **1.4 Open questions**

Decrire le m  
Regarder th  
Kochebina  
Limite du n  
Interessant,  
les neutrino  
CP ? Pb des



<sup>67</sup> **Chapter 2**

<sup>68</sup> **The JUNO experiment**

<sup>69</sup> “Ave Juno, rosae rosam, et spiritus rex”. It means nothing but I found it in tone.

<sup>70</sup> The first idea of a medium baseline ( $\sim 52$  km) experiment, was explored in 2008 [1] where it was <sup>71</sup> demonstrated that the Neutrino Mass Ordering (NMO) could be determined by a medium baseline <sup>72</sup> experiment if  $\sin^2(2\theta_{13}) > 0.005$  without the requirements of accurate knowledge of the reactor <sup>73</sup> antineutrino spectra and the value of  $\Delta m_{32}^2$ . From this idea is born the Jiangmen Underground <sup>74</sup> Neutrino Observatory (JUNO) experiment.

<sup>75</sup> JUNO is a neutrino detection experiment under construction located in China, in Guangdong <sup>76</sup> proving, near the city of Kaiping. Its main objectives are the determination of the mass ordering <sup>77</sup> at the  $3-4\sigma$  level in 6 years of data taking and the measurement at the sub-percent precision of the <sup>78</sup> oscillation parameters  $\Delta m_{21}^2$ ,  $\sin^2 \theta_{12}$ ,  $\Delta m_{32}^2$  and with less precision  $\sin^2 \theta_{13}$ [2].



FIGURE 2.1 – On the left: Location of the JUNO experiment and its reactor sources in southern china. On the right: Aerial view of the experimental site

<sup>79</sup> For this JUNO will measure the electronic anti-neutrinos ( $\bar{\nu}_e$ ) flux coming from the nuclear reactors of <sup>80</sup> Taishan, Yangjiang, for a total power of  $26.6 \text{ GW}_{th}$ , and the Daya Bay power plant to a lesser <sup>81</sup> extent. All of those cores are the second-generation pressurized water reactors CPR1000, which is a <sup>82</sup> derivative of Framatome M310. Details about the power plants characteristics and their expected flux <sup>83</sup> of  $\bar{\nu}_e$  can be found in the table 2.1. The distance of 53 km has been specifically chosen to maximize <sup>84</sup> the disappearance probability of the  $\bar{\nu}_e$ . The data taking is scheduled to start early 2025.

<sup>85</sup> **2.1 Neutrinos physics in JUNO**

<sup>86</sup> Even if the JUNO design detailed in section 2.2 was optimized for the measurement of the NMO, <sup>87</sup> its large detection volume, excellent energy resolution and background level and understanding <sup>88</sup> make it also an excellent detector to measure the flux coming from other neutrino sources. Thus

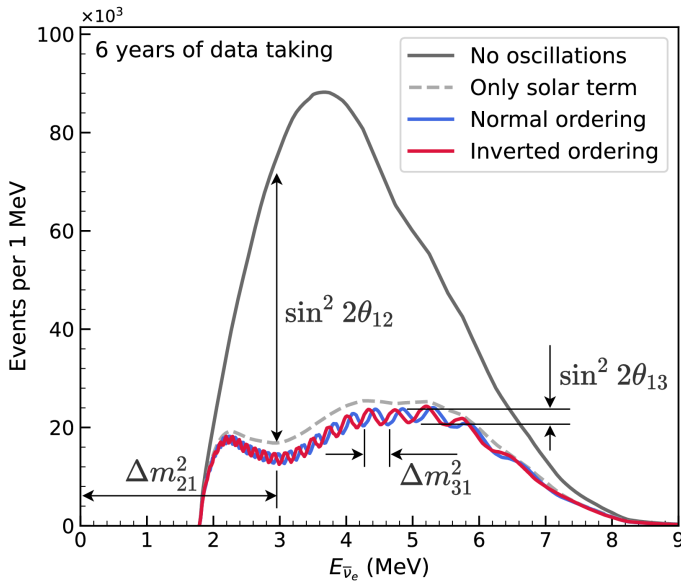


FIGURE 2.2 – Expected number of neutrinos event per MeV in JUNO after 6 years of data taking. The black curve shows the flux if there was no oscillation. The light gray curve shows the oscillation if only the solar terms are taken in account ( $\theta_{12}$ ,  $\Delta m_{21}^2$ ). The blue and red curve shows the spectrum in the case of, respectively, NO and IO. The dependency of the oscillation to the different parameters are schematized by the double sided arrows. We can see the NMO sensitivity by looking at the fine phase shift between the red and the blue curve.

89 the scientific program of JUNO extends way over reactor antineutrinos. The following section is an  
90 overview of the different physics topic JUNO will contribute in the coming years.

### 91 2.1.1 Reactor neutrino oscillation for NMO and precise measurements

Previous works [1, 3] shows that oscillation parameters and the NMO can be observed by looking at the  $\bar{\nu}_e$  disappearance energy spectrum coming from medium baseline nuclear reactor. This disappearance probability can be expressed as [2] :

$$P(\bar{\nu}_e \rightarrow \bar{\nu}_e) = 1 - \sin^2 2\theta_{12} c_{13}^4 \sin^2 \frac{\Delta m_{21}^2 L}{4E} - \sin^2 2\theta_{13} \left[ c_{12}^2 \sin^2 \frac{\Delta m_{31}^2 L}{4E} + s_{12}^2 \sin^2 \frac{\Delta m_{32}^2 L}{4E} \right]$$

92 Where  $s_{ij} = \sin \theta_{ij}$ ,  $c_{ij} = \cos \theta_{ij}$ ,  $E$  is the  $\bar{\nu}_e$  energy and  $L$  is the baseline. We can see the sensitivity  
93 to the NMO in the dependency to  $\Delta m_{32}^2$  and  $\Delta m_{31}^2$  causing a phase shift of the spectrum as we can  
94 see in the figure 2.2. By carefully adjusting a theoretical spectrum to the data, one can extract the  
95 NMO and the oscillation parameters. The statistic procedure used to adjust the theoretical spectrum  
96 is reviewed in more details in the section 2.7. To reach the desired sensitivity, JUNO must meet  
97 multiple requirements but most notably:

- 98 1. An energy resolution of  $3\% / \sqrt{E(\text{MeV})}$  to be able to distinguish the fine structure of the fast  
99 oscillation.
- 100 2. An energy precision of 1% in order to not err on the location of the oscillation pattern.
- 101 3. A baseline of  $53 \pm 0.5$  km to maximise the  $\bar{\nu}_e$  oscillation probability.
- 102 4. At least  $\approx 100,000$  events to limit the spectrum distortion due to statistical uncertainties.

103  **$\bar{\nu}_e$  flux coming from nuclear power plants**

104 To get such high measurements precision, it is necessary to have a very good understanding of  
 105 the sources characteristics. For its NMO and precise measurement studies, JUNO will observe the  
 106 energy spectrum of neutrinos coming from the nuclear power plants Taishan and Yangjiang's cores,  
 107 located at 53 km of the detector to maximise the disappearance probability of the  $\bar{\nu}_e$ .

Reactor	Power (GW <sub>th</sub> )	Baseline (km)	IBD Rate (day <sup>-1</sup> )	Relative Flux (%)
Taishan	9.2	52.71	15.1	32.1
Core 1	4.6	52.77	7.5	16.0
Core 2	4.6	52.64	7.6	16.1
Yangjiang	17.4	52.46	29.0	61.5
Core 1	2.9	52.74	4.8	10.1
Core 2	2.9	52.82	4.7	10.1
Core 3	2.9	52.41	4.8	10.3
Core 4	2.9	52.49	4.8	10.2
Core 5	2.9	52.11	4.9	10.4
Core 6	2.9	52.19	4.9	10.4
Daya Bay	17.4	215	3.0	6.4

TABLE 2.1 – Characteristics of the nuclear power plants observed by JUNO. The IBD rate are estimated from the baselines, the reactors full thermal power, selection efficiency and the current knowledge of the oscillation parameters

108 The  $\bar{\nu}_e$  coming from reactors are emitted from  $\beta$ -decay of unstable fission fragments. The Taishan  
 109 and Yangjiang reactors are Pressurised Water Reactor (PWR), the same type as Daya Bay. In those  
 110 type of reactor more the 99.7 % and  $\bar{\nu}_e$  are produced by the fissions of four fuel isotopes <sup>235</sup>U, <sup>238</sup>U,  
 111 <sup>239</sup>Pu and <sup>241</sup>Pu. The neutrino flux per fission of each isotope is determined by the inversion of the  
 112 measured  $\beta$  spectra of fission product [4–8] or by calculation using the nuclear databases [9, 10].

113 The neutrino flux coming from a reactor at a time  $t$  can be predicted using

$$\phi(E_\nu, t)_r = \frac{W_{th}(t)}{\sum_i f_i(t) e_i} \sum_i f_i(t) S_i(E_\nu) \quad (2.1)$$

114 where  $W_{th}(t)$  is the thermal power of the reactor,  $f_i(t)$  is the fraction fission of the  $i$ th isotope,  $e_i$  its  
 115 thermal energy released in each fission and  $S_i(e_\nu)$  the neutrino flux per fission for this isotope. Using  
 116 this method, the flux uncertainty is expected to be of an order of 2-3 % [11].

117 In addition to those prediction, a satellite experiment named TAO[12] will be setup near the  
 118 reactor core Taishan-1 to measure with an energy resolution of 2% at 1 MeV the neutrino flux coming  
 119 from the core, more details can be found in section 2.4.1. It will help identifying unknown fine  
 120 structure and give more insight on the  $\bar{\nu}_e$  flux coming from this reactor.

121 One the open issue about reactor anti-neutrinos flux is the so-called neutrino anomaly [13], an  
 122 unexpected surplus of neutrino emission in the spectra around 5 MeV. Multiples scientists are trying  
 123 to explain this surplus by advanced recalculation of the nuclei model during beta decay [14, 15] but  
 124 no consensus on this issue has been reached yet.

125 **Background in the neutrinos reactor spectrum**

126 Considering the close reactor neutrinos flux as the main signal, the signals that are considered as  
 127 background are:

- 128 — The geoneutrinos producing background in the 0.511 ~ 2.7 MeV region.
- 129 — The neutrinos coming from the other nuclear reactors around Earth.

130 In addition to all those physics signal, non-neutrinos signal that would mimic an IBD will also be  
 131 present. It is composed of:

- The signal coming from radioactive decay ( $\alpha$ ,  $\gamma$ ,  $\beta$ ) from natural radioactive isotopes in the material of the detector.
- Cosmogenic event such as fast neutrons and activated isotopes induced by muons passing through the detector, most notably the spallation on  $^{12}\text{C}$ .
- All those events represent a non-negligible part of the spectrum as shown in figure 2.3.

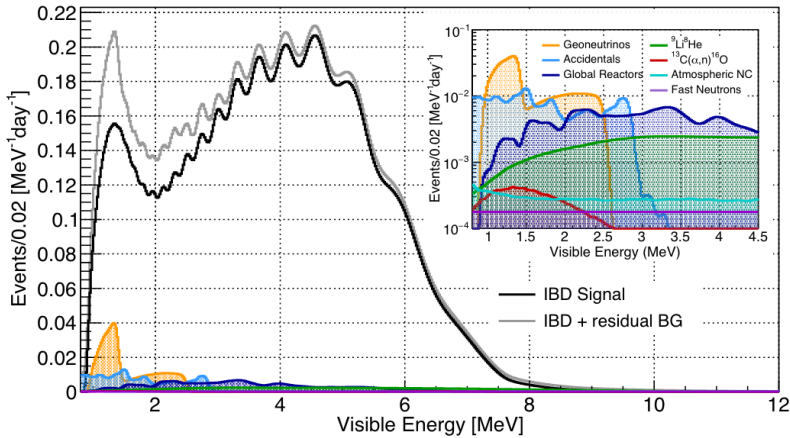


FIGURE 2.3 – Expected visible energy spectrum measured with the LPMT system with (grey) and without (black) backgrounds. The background amount for about 7% of the IBD candidate and are mostly localized below 3 MeV [11]

### 137 Identification of the mass ordering

138 To identify the mass ordering, we adjust the theoretical neutrino energy spectrum under the  
 139 two hypothesis of NO and IO. Those give us two  $\chi^2$ , respectively  $\chi^2_{NO}$  and  $\chi^2_{IO}$ . By computing the  
 140 difference  $\Delta\chi^2 = \chi^2_{NO} - \chi^2_{IO}$  we can determine the most probable mass ordering and the confidence  
 141 interval: NO if  $\Delta\chi^2 > 0$  and IO if  $\Delta\chi^2 < 0$ . Current studies shows that the expected sensitivity  
 142 the mass ordering would be of  $3.4\sigma$  after 6 years of data taking in nominal setup[2]. More detailed  
 143 explanations about the procedure can be found in the section 2.7.

### 144 Precise measurement of the oscillations parameters

145 The oscillations parameters  $\theta_{12}$ ,  $\theta_{13}$ ,  $\Delta m_{21}^2$ ,  $\Delta m_{31}^2$  are free parameters in the fit of the oscillation  
 146 spectrum. The precision on those parameters have been estimated and are shown in table 2.2. Wee  
 147 see that for  $\theta_{12}$ ,  $\Delta m_{21}^2$ ,  $\Delta m_{31}^2$ , precision at 6 years is better than the reference precision by an order of  
 148 magnitude [11]

	Central Value	PDG 2020	100 days	6 years	20 years
$\Delta m_{31}^2 (\times 10^{-3} \text{ eV}^2)$	2.5283	$\pm 0.034$ (1.3%)	$\pm 0.021$ (0.8%)	$\pm 0.0047$ (0.2%)	$\pm 0.0029$ (0.1%)
$\Delta m_{21}^2 (\times 10^{-3} \text{ eV}^2)$	7.53	$\pm 0.18$ (2.4%)	$\pm 0.074$ (1.0%)	$\pm 0.024$ (0.3%)	$\pm 0.017$ (0.2%)
$\sin^2 \theta_{12}$	0.307	$\pm 0.013$ (4.2%)	$\pm 0.0058$ (1.9%)	$\pm 0.0016$ (0.5%)	$\pm 0.0010$ (0.3%)
$\sin^2 \theta_{13}$	0.0218	$\pm 0.0007$ (3.2%)	$\pm 0.010$ (47.9%)	$\pm 0.0026$ (12.1%)	$\pm 0.0016$ (7.3%)

TABLE 2.2 – A summary of precision levels fir the oscillation parameters. The reference value (PDG 2020 [16]) is compared with 100 days, 6 years and 20 years of JUNO data taking.

### 2.1.2 Other physics

While the design of JUNO is tailored to measure  $\bar{\nu}_e$  coming from nuclear reactor, JUNO will be able to detect neutrinos coming from other sources thus allowing for a wide range of physics studies as detailed in the table 2.3 and in the following sub-sections.

Research	Expected signal	Energy region	Major backgrounds
Reactor antineutrino	60 IBDs/day	0–12 MeV	Radioactivity, cosmic muon
Supernova burst	5000 IBDs at 10 kpc 2300 elastic scattering	0–80 MeV	Negligible
DSNB (w/o PSD)	2–4 IBDs/year	10–40 MeV	Atmospheric $\nu$
Solar neutrino	hundreds per year for $^8B$	0–16 MeV	Radioactivity
Atmospheric neutrino	hundreds per year	0.1–100 GeV	Negligible
Geoneutrino	$\approx 400$ per year	0–3 MeV	Reactor $\nu$

TABLE 2.3 – Detectable neutrino signal in JUNO and the expected signal rates and major background sources

### 153 Geoneutrinos

154 Geoneutrinos designate the antineutrinos coming from the decay of long-lived radioactive elements inside the Earth. The 1.8 MeV threshold necessary for the IBD makes it possible to measure  
 155 geoneutrinos from  $^{238}\text{U}$  and  $^{232}\text{Th}$  decay chains. The studies of geoneutrinos can help refine the Earth  
 156 crust models but is also necessary to characterise their signal, as they are a background to the mass  
 157 ordering and oscillations parameters studies.

### 159 Atmospheric neutrinos

160 Atmospheric neutrinos are neutrinos originating from the decay of  $\pi$  and  $K$  particles that are  
 161 produced in extensive air showers initiated by the interactions of cosmic rays with the Earth atmosphere.  
 162 Earth is mostly transparent to neutrinos below the PeV energy, thus JUNO will be able to  
 163 see neutrinos coming from all directions. Their baseline range is large (15km  $\sim$  13000km), they can  
 164 have energy between 0.1 GeV and 10 TeV and will contain all neutrino and antineutrinos flavour.  
 165 Their studies is complementary to the reactor antineutrinos and can help refine the constraints on  
 166 the NMO [2].

### 167 Supernovae burst neutrinos

168 Neutrinos are crucial component during all stages of stellar collapse and explosion. Detection  
 169 of neutrinos coming for core collapse supernovae will provide us important informations on the  
 170 mechanisms at play in those events. Thanks to its 20 kt sensible volume, JUNO has excellent capabilities  
 171 to detect all flavour of the  $\mathcal{O}(10 \text{ MeV})$  postshock neutrinos, and using neutrinos of the  $\mathcal{O}(1 \text{ MeV})$   
 172 will give informations about the pre-supernovae neutrinos. All those informations will allow  
 173 to disentangle between the multiple hydro-dynamic models that are currently used to describe the  
 174 different stage of core-collapse supernovae.

### 175 Diffuse supernovae neutrinos background

176 Core-collapse supernovae in our galaxy are rare events, but they frequently occur throughout the  
 177 visible Universe sending burst of neutrinos in direction of the Earth. All those events contributes to  
 178 a low background flux of low-energy neutrinos called the Diffuse Supernovae Neutrino Background  
 179 (DSNB). Its flux and spectrum contains informations about the red-shift dependent supernovae rate,

180 the average supernovae neutrino energy and the fraction of black-hole formation in core-collapse supernovae. Depending of the DSNB model, we can expect 2-4 IBD events per year in the energy range  
 181 above the reactor  $\bar{\nu}_e$  signal, which is competitive with the current Super-Kamiokande+Gadolinium  
 182 phase [17].  
 183

#### 184 Beyond standard model neutrinos interactions

185 JUNO will also be able to probe for beyond standard model neutrinos interactions. After the  
 186 main physics topics have been accomplished, JUNO could be upgraded to probe for neutrinoless  
 187 beta decay ( $0\nu\beta\beta$ ). The detection of such event would give critical informations about the nature  
 188 of neutrinos, is it a majorana or a dirac particle. JUNO will also be able to probe for neutrinos that  
 189 would come for the decay or annihilation of Dark Matter inside the sun and neutrinos from putative  
 190 primordial black hole. Through the unitary test of the mixing matrix, JUNO will be able to search  
 191 for light sterile neutrinos. Thanks to JUNO sensitivity, multiple other exotic can be performed on  
 192 neutrino related beyond standard model interactions.

## 193 2.2 The JUNO detector

194 The JUNO detector is a scintillator detector buried 693.35 meters under the ground (1800 meters  
 195 water equivalent). It consist of Central Detector (CD), a water pool and a Top Tracker (TT) as showed  
 196 in figure 2.4a. The CD is an acrylic vessel containing the 20 ktons of Liquid Scintillator (LS). It is  
 197 supported by a stainless steel structure and is immersed in that water pool that is used as shielding  
 198 from external radiation and as a cherenkov detector for the background. The top of the experiment  
 199 is partially covered by the Top Tracker (TT), a plastic scintillator detector which is use to detect the  
 200 atmospheric muons background and is acting as a veto detector.

201 The top of the experiment also host the LS purification system, a water purification system, a  
 202 ventilation system to get rid of the potential radon in the air. The CD is observed by two system of  
 203 Photo-Multipliers Tubes (PMT). They are attached to the steel structure and their electronic readout  
 204 is submersed near them. A third system of PMT is also installed on the structure but are facing  
 205 outward of the CD, instrumenting the water to be cherenkov detector. The CD and the cherenkov  
 206 detector are optically separated by Tyvek sheet. A chimney for LS filling and purification and for  
 207 calibration operations connects the CD to the experimental hall from the top.

208 The CD has been dimensioned to meet the requirements presented in section 2.1.1:

- 209 — Its 20 ktons monolithic LS provide a volume sizeable enough, in combination with the ex-  
 210 pected  $\bar{\nu}_e$  flux, to reach the desired statistic in 6 years. Its monolithic nature also allow for a  
 211 full containment of most of the events, preventing the energy loss in non-instrumented parts  
 212 that would arise from a segmented detector.
- 213 — Its large overburden shield it from most of the atmospheric background that would pollute  
 214 the signal.
- 215 — The localization of the experiment, chosen to maximize the disappearance with a 53km base-  
 216 line and in a region that allow two nuclear power plant to be used as sources.

217 This section cover in details the different components of the detector and the detection systems.

### 218 2.2.1 Detection principle

The CD will detect the neutrino and measure their energy mainly via an Inverse Beta Decay (IBD) interaction with proton mainly from the  $^{12}\text{C}$  and H nucleus in the LS:

$$\bar{\nu}_e + p \rightarrow n + e^+$$

219 Kinematics calculation shows that this interaction has an energy threshold for the  $\bar{\nu}_e$  of  $(m_n + m_e -$   
 220  $m_p) \approx 1.806 \text{ MeV}$  [18] where  $m_\lambda$  is the mass of the  $\lambda$  particle. This threshold make the experiment

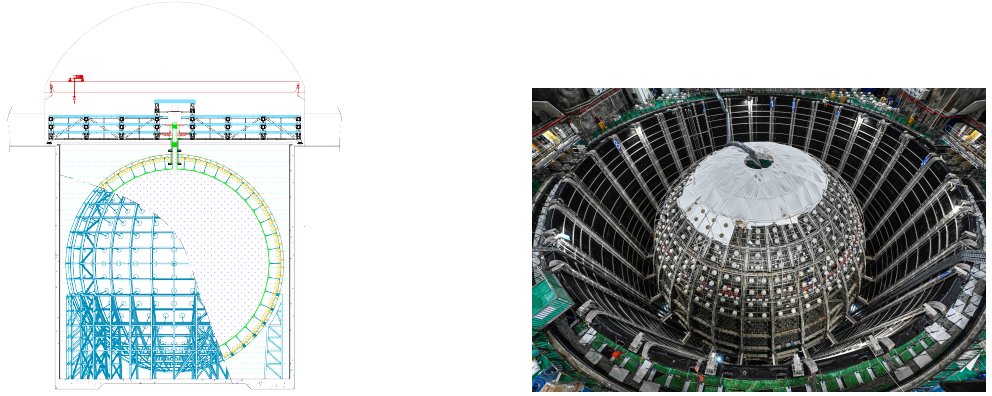


FIGURE 2.4

blind to very low energy neutrinos. The residual energy  $E_\nu - 1.806$  MeV is distributed as kinetic energy between the positron and the neutron. The energy of the emitted positron  $E_e$  is given by [18]

$$E_e = \frac{(E_\nu - \delta)(1 + \epsilon_\nu) + \epsilon_\nu \cos \theta \sqrt{(E_\nu - \delta)^2 + \kappa m_e^2}}{\kappa} \quad (2.2)$$

where  $\kappa = (1 + \epsilon_\nu)^2 - \epsilon_\nu^2 \cos^2 \theta \approx 1$ ,  $\epsilon_\nu = \frac{E_\nu}{m_p} \ll 1$  and  $\delta = \frac{m_n^2 - m_p^2 - m_e^2}{2m_p} \ll 1$ . We can see from this equation that the positron energy is strongly correlated to the neutrino energy.

The positron and the neutron will then propagate in the detection medium, the Liquid Scintillator (LS), loosing their kinetic energy by exciting the molecule of the LS (more details in section 2.2.2). Once stopped, the positron will annihilate with an electron from the medium producing two 511 KeV gamma. Those gamma will themselves interact with the LS, exciting it before being absorbed by photoelectrical effect. The neutron will be captured by an hydrogen, emitting a 2.2 MeV gamma in the process. This gamma will also deposit its energy before being absorbed by the LS.

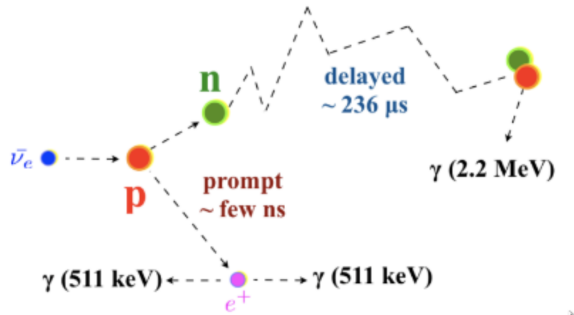


FIGURE 2.5 – Schematics of an IBD interaction in the central detector of JUNO

The scintillation photons have frequency in the UV and will propagate in the LS, being re-absorbed and re-emitted by compton effect before finally be captured by PMTs instrumenting the acrylic sphere. The analog signal of the PMTs digitized by the electronic is the signal of our experiment. The signal produced by the positron is subsequently called the prompt signal, and the signal coming from the neutron the delayed signal. This naming convention come from the fact that the positron will deposit its energy rather quickly (few ns) where the neutron will take a bit more time ( $\sim 236$   $\mu$ s).

### 237 2.2.2 Central Detector (CD)

238 The central detector, composed of 20 ktons of Liquid Scintillator (LS), is the main part of JUNO.  
 239 The LS is contained in a spherical acrylic vessel supported by a stainless steel structure. The CD and  
 240 its structural support are submerged in a cylindrical water pool of 43.5m diameter and 44m height.  
 241 We're confident that the water pool provide sufficient buffer protection in every direction against the  
 242 rock radioactivity.

#### 243 Acrylic vessel

244 The acrylic vessel is a spherical vessel of inner diameter of 35.4 m and a thickness of 120 mm. It  
 245 is assembled from 265 acrylic panels, thermo bonded together. The acrylic recipes has been carefully  
 246 tuned with extensive R&D to ensure it does not include plasticizer and anti-UV material that would  
 247 stop the scintillation photons. Those panels requires to be pure of radioactive materials to not  
 248 cause background. Current setup where the acrylic panels are molded in cleanrooms of class 10000,  
 249 let us reach a uranium and thorium contamination of <0.5 ppt. The molding and thermoforming  
 250 processes is optimized to increase the assemblage transparency in water to >96%. The acrylic vessel  
 251 is supported by a stainless steel structure via supporting node (fig 2.6). The structure and the nodes  
 252 are designed to be resilient to natural catastrophic events such as earthquake and can support many  
 253 times the effective load of the acrylic vessel.

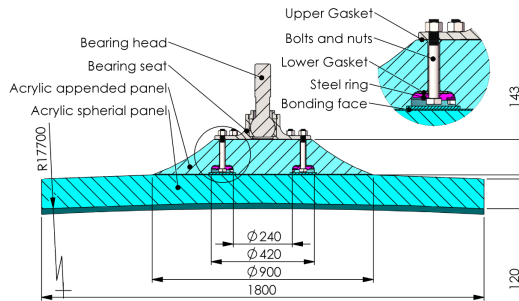


FIGURE 2.6 – Schematics of the supporting node for the acrylic vessel

#### 254 Liquid scintillator

255 The Liquid Scintillator (LS) has a similar recipe as the one used in Daya Bay [19] but without  
 256 gadolinium doping. It is made of three components, necessary to shift the wavelength of emitted  
 257 photons to prevent their reabsorption:

- 258 1. The detection medium, the *linear alkylbenzene* (LAB). Selected because of its excellent trans-  
 259 parency, high flash point, low chemical reactivity and good light yield. Accounting for  $\sim$   
 260 98% of the LS, it is the main component with which ionizing particles and gamma interact.  
 261 Charged particles will collide with its electronic cloud transferring energy to the molecules,  
 262 gamma will interact via compton effect with the electronic cloud before finally be absorbed  
 263 via photoelectric effect.
- 264 2. The second component of the LS is the *2,5-diphenyloxazole* (PPO). A fraction of the excitation  
 265 energy of the LAB is transferred to the PPO, mainly via non radiative process [20]. The  
 266 PPO molecules de-excites in the same way, transferring their energy to the bis-MSB. The PPO  
 267 makes for 1.5 % of the LS.
- 268 3. The last component is the *p-bis(o-methylstyryl)-benzene* (bis-MSB). Once excited by the PPO, it  
 269 will emit photon with an average wavelength of  $\sim$  430 nm (full spectrum in figure 2.7) that  
 270 can be detected by our photo-multipliers systems. It amount for  $\sim$  0.5% of the LS.

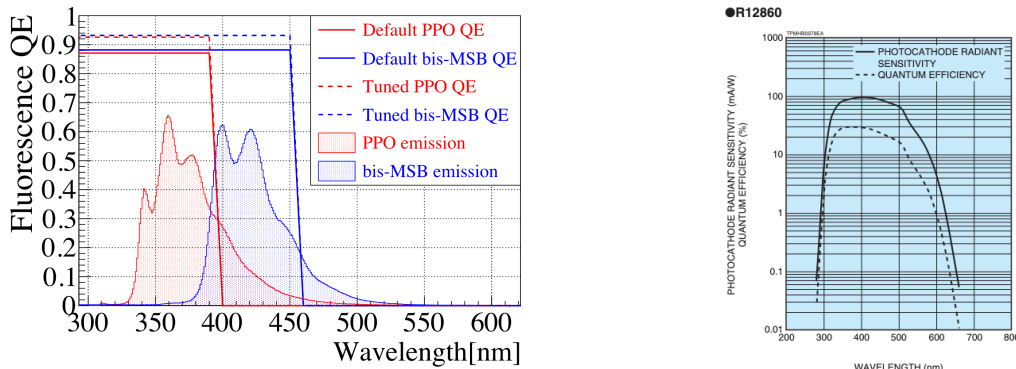


FIGURE 2.7 – On the left: Quantum efficiency (QE) and emission spectrum of the LAB and the bis-MSB [19]. On the right: Sensitivity of the Hamamatsu LPMT depending on the wavelength of the incident photons [21].

This formula has been optimized using dedicated studies with a Daya Bay detector [19, 22] to reach the requirements for the JUNO experiment:

- A light yield / MeV of the amount of  $10^4$  photons to maximize the statistic in the energy measurement.
- An attenuation length comparable to the size of the detector to prevent losing photons during their propagation in the LS. The final attenuation length is 25.8m [23] to compare with the CD diameter of 35.4m.
- Uranium/Thorium radiopurity to prevent background signal. The reactor neutrino program require a contamination fraction  $F < 10^{-15}$  while the solar neutrino program require  $F < 10^{-17}$ .

The LS will frequently be purified and tested in the Online Scintillator Internal Radioactivity Investigation System (OSIRIS) [24] to ensure that the requirements are kept during the lifetime of the experiment, more details to be found in section 2.4.2.

#### 284 Large Photo-Multipliers Tubes (PMTs)

The scintillation light produced by the LS is then collected by Photo-Multipliers Tubes (PMT) that transform the incoming photon into an electric signal. As described in figure 2.8, the incident photons interact with the photocathode via photoelectric effect producing an electron called a Photo-Electron (PE). This PE is then focused on the dynodes where the high voltage will allow it to be multiplied. After multiple amplification the resulting charge - in coulomb [C] - is collected by the anode and the resulting electric signal can be digitalized by the readout electronics from which the charge and timing can be extracted.

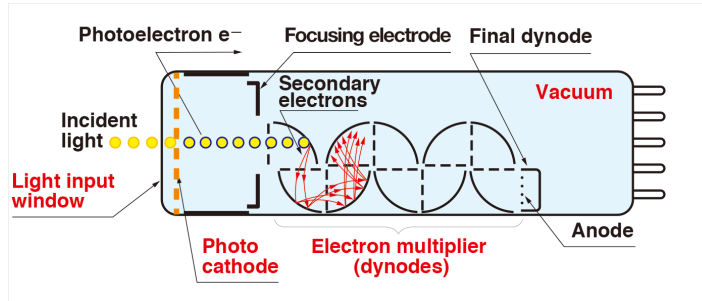


FIGURE 2.8 – Schematic of a PMT

The Large Photo-Multipliers Tubes (LPMT), used in the central detector and in the water pool, are 20-inch (50.8 cm) radius PMTs.  $\sim 5000$  dynode-PMTs [21] were produced by the Hamamatsu<sup>©</sup> company and  $\sim 15000$  Micro-Channel Plate (MCP) [25] by the NNVT<sup>©</sup> company. This system is the one responsible for the energy measurement with a energy resolution of  $3\%/\sqrt{E}$ , resolution necessary for the mass ordering measurement. To reach this precision, the system is composed of 17612 PMTs quasi uniformly distributed over the detector for a coverage of 75.2% reaching  $\sim 1800$  PE/MeV or  $\sim 2.3\%$  resolution due to statistic, leaving  $\sim 0.7\%$  for the systematic uncertainties. They are located outside the acrylic sphere in the water pool facing the center of the detector. To maintain the resolution over the lifetime of the experiment, JUNO require a failure rate  $< 1\%$  over 6 years.

The LPMTs electronic are divided in two parts. One "near", located underwater, in proximity of the LPMT to reduce the cable length between the PMT and early electronic. A second one, outside of the detector that is responsible for higher level analysis before sending the data to the DAQ.

The light yield per MeV induce that a LPMT can collect between 1 and 1000 PE per event, causing non linearity in the PMT response that need to be understood and calibrated, see section 2.3 for more details.

### Small Photo-Multipliers Tubes (SPMTs)

The Small PMT (SPMTs) system is made of 3-inch (7.62 cm) PMTs. They will be used in the CD as a secondary detection system. Those 25600 SPMTs will observe the same events as the LPMTs, thus sharing the physics and detector systematics up until the photon conversion. With a detector coverage of 2.7%, this system will collect  $\sim 43$  PE/MeV for a final energy resolution of  $\sim 17\%$ . This resolution is not enough to measure the NMO,  $\theta_{13}$ ,  $\Delta m_{31}^2$  but will be sufficient to independently measure  $\theta_{12}$  and  $\Delta m_{21}^2$ .

Due to the low PE rate, SPMTs will be running in photo-counting mode in the reactor range and thus will be insensitive to non-linearity effect. Using this property, the intrinsic charge non linearity of the LPMTs can be measured by comparing the PE count in the SPMTs and LPMTs [26]. Also, due to their smaller size and electronics, SPMTs have a better timing resolutions than the LPMTs. At higher energy range, like supernovae events, LPMTs will saturate where SPMTs due to their lower PE collection will to produce a reliable measure of the energy spectrum.

The Data Acquisition System (DAQ) is designed to support the event rate of IBD, background, dark noise and supplementary storage buffers are present in the LPMT electronics to withstand the event rate during supernovae burst.

### 2.2.3 Veto detector

The CD will be bathed in constant background noise coming from numerous sources : the radioactivity from surrounding rock and its own components or from the flux of cosmic muons. This background needs to be rejected to ensure the purity of the IBD spectrum. To prevent a big part of them, JUNO use two veto detector that will tag events as background before CD analysis.

### Cherenkov in water pool

The Water Cherenkov Detector (WCD) is the instrumentation of the water buffer around the CD. When high speed charged particles will pass through the water, they will produced cherenkov photons. The light will be collected by 2400 MCP LPMTs installed on the outer surface of the CD structure. The muons veto strategy is based on a PMT multiplicity condition. WCD PMTs are grouped in ten zones: 5 in the top, 5 in the bottom. A veto is raised either when more than 19 PMTs are triggered in one zone or when two adjacent zones simultaneously trigger more than 13 PMTs. Using this trigger, we expect to reach a muon detection efficiency of 99.5% while keeping the noise at reasonable level.

337 **Top tracker**

338 The JUNO Top Tracker (TT) is a plastic scintillator detector located on the top of the experiment  
 339 (see figure 2.9). Made from plastic scintillator from OPERA [27] layered horizontally in 3 layers on  
 340 the top of the detector, the TT will be able to detect incoming atmospheric muons. With its coverage,  
 341 about 1/3 of the of all atmospheric muons that passing through the CD will also pass through the 3  
 342 layer of the detector. While it does not cover the majority of the CD, the TT is particularly effective  
 343 to detect muons coming through the filling chimney region which might present difficulties from the  
 other subsystems in some classes of events.

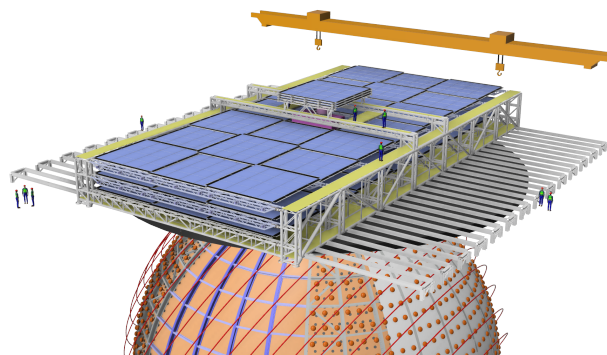


FIGURE 2.9 – The JUNO top tracker

344

345 **2.3 Calibration strategy**

346 The calibration is a crucial part of the JUNO experiment. Because we are looking at civil reactor  
 347 neutrino it might be impossible to run measurement without signal, it would need to shut down  
 348 every reactor from the Taishan and Yangjiang power plants which is realistically impossible. Because  
 349 of this continuous rate, low frequency signal event, we need high frequency, recognisable sources in  
 350 the energy range of interest : [0-12] MeV for the positron signal and 2.2 MeV for the neutron capture.  
 351 It is expected that the CD response will be different depending on the type of particle, due to the  
 352 interaction with LS, the position on the event and the optical response of the acrylic sphere (see  
 353 section 2.6). We also expect a non-linear energy response of the CD due to the LS properties [19] but  
 354 also due to the saturation of the LPMTs system when collecting a large amount of PE [26].

355

### 2.3.1 Energy scale calibration

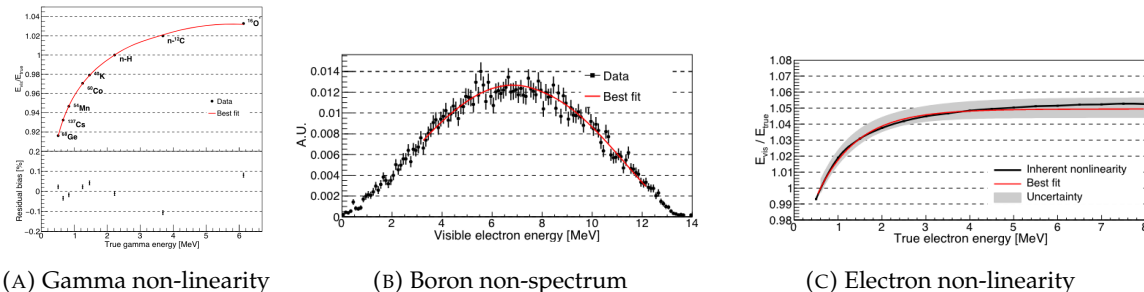
356 While electrons and positrons sources would be ideal, for a large LS detector thin-walled electrons  
 357 or positrons sources could lead to leakage of radionucleides causing radioactive contamination.  
 358 Instead, we consider gamma sources in the range of the prompt energy of IBDs. The sources are  
 359 reported in table 2.4.

360 For the  $^{68}\text{Ge}$  source, it will decay in  $^{68}\text{Ga}$  via electron capture, which will itself  $\beta^+$  decay into  $^{68}\text{Zn}$ .  
 361 The positrons will be absorbed by the enclosure so only the annihilation gamma will be released. In  
 362 addition,  $(\alpha, n)$  sources like  $^{241}\text{Am-Be}$  and  $^{241}\text{Am-}^{13}\text{C}$  are used to provide both high energy gamma  
 363 and neutrons, which will later be captured in the LS producing the 2.2 MeV gamma.

364 From this calibration we call  $E_{\text{vis}}$  the "visible energy" that is reconstructed by our current algo-  
 365 rithms and we compare it to the true energy deposited by the calibration source. The results shown  
 366 in figure 2.10 show the expected response of the detector from calibration sources. The non-linearity  
 367 is clearly visible from the  $E_{\text{vis}}/E_{\text{true}}$  shape. See [28] for more details.

Sources / Processes	Type	Radiation
$^{137}\text{Cs}$	$\gamma$	0.0662 MeV
$^{54}\text{Mn}$	$\gamma$	0.835 MeV
$^{60}\text{Co}$	$\gamma$	$1.173 + 1.333$ MeV
$^{40}\text{K}$	$\gamma$	1.461 MeV
$^{68}\text{Ge}$	$e^+$	annihilation 0.511 + 0.511 MeV
$^{241}\text{Am-Be}$	$n, \gamma$	neutron + 4.43 MeV ( $^{12}\text{C}^*$ )
$^{241}\text{Am-}^{13}\text{C}$	$n, \gamma$	neutron + 6.13 MeV ( $^{16}\text{O}^*$ )
$(n, \gamma)p$	$\gamma$	2.22 MeV
$(n, \gamma)^{12}\text{C}$	$\gamma$	4.94 MeV or 3.68 + 1.26 MeV

TABLE 2.4 – List of sources and their process considered for the energy scale calibration

FIGURE 2.10 – Fitted and simulated non linearity of gamma, electron sources and from the  $^{12}\text{B}$  spectrum. Black points are simulated data. Red curves are the best fits

### 2.3.2 Calibration system

The non-uniformity due to the event position in the detector (more details in section 2.6) will be studied using multiples systems that are schematized in figure 2.11. They allow to position sources at different location in the CD.

- For a one-dimension vertical calibration, the Automatic Calibration Unit (ACU) will be able to deploy multiple radioactive sources or a pulse laser diffuser ball along the central axis of the CD through the top chimney. The source position precision is less than 1cm.
- For off-axis calibration, a calibration source attached to a Cable Loop System (CLS) can be moved on a vertical half-plane by adjusting the length of two connection cable. Two set of CSL will be deployed to provide a 79% effective coverage of a vertical plane.
- A Guiding Tube (GT) will surround the CD to calibrate the non-uniformity of the response at the edge of the detector
- A Remotely Operated under-LS Vehicle (ROV) can be deployed to desired location inside LS for a more precise and comprehensive calibration. The ROV will also be equipped with a camera for inspection of the CD.

The preliminary calibration program is depicted in table 2.5.

## 2.4 Satellite detectors

As introduced in section 2.1.1 and section 2.2.2, the precise knowledge and understanding of the detector condition is crucial for the measurements of the NMO and oscillation parameters. Thus two satellite detectors will be setup to monitor the experiment condition. TAO to monitor and understand the  $\bar{\nu}_e$  flux and spectrum coming from the nuclear reactor and OSIRIS to monitor the LS response.

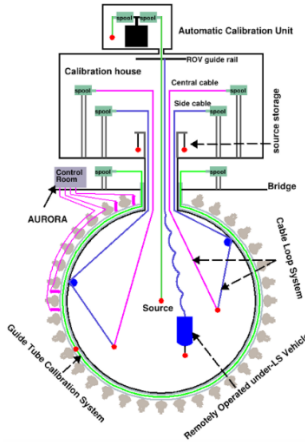


FIGURE 2.11 – Overview of the calibration system

Program	Purpose	System	Duration [min]
Weekly calibration	Neutron (Am-C)	ACU	63
	Laser	ACU	78
Monthly calibration	Neutron (Am-C)	ACU	120
	Laser	ACU	147
	Neutron (Am-C)	CLS	333
	Neutron (Am-C)	GT	73
Comprehensive calibration	Neutron (Am-C)	ACU, CLS and GT	1942
	Neutron (Am-Be)	ACU	75
	Laser	ACU	391
	$^{68}\text{Ge}$	ACU	75
	$^{137}\text{Cs}$	ACU	75
	$^{54}\text{Mn}$	ACU	75
	$^{60}\text{Co}$	ACU	75
	$^{40}\text{K}$	ACU	158

TABLE 2.5 – Calibration program of the JUNO experiment

### 2.4.1 TAO

The Taishan Antineutrino Observatory (TAO) [12, 29] is a ton-level gadolinium doped liquid scintillator detector that will be located near the Taishan-1 reactor. It aim to measure the  $\bar{\nu}_e$  spectrum at very low distance ( $< 30\text{m}$ ) from the reactor to measure a quasi-unoscillated spectrum. TAO also aim to provide a major contribution to the so-called reactor anomaly [13]. Its requirement are to the level of 2 % energy resolution at 1 MeV.

#### Detector

The TAO detector is close, in concept, to the CD of JUNO. It is composed of an acrylic vessel containing 2.8 tons of gadolinium-loaded LS instrumented by an array of silicon photomultipliers (SiPM) reaching a 95% coverage. To efficiently reduce the dark count of those sensors, the detector is cooled to  $-50\text{ }^\circ\text{C}$ . The  $\bar{\nu}_e$  will interact with the LS via IBD, producing scintillation light, that will be detected by the SiPMs. From this signal the  $\bar{\nu}_e$  energy and the full spectrum reconstructed. This spectrum will then be used by JUNO to calibrate the unoscillated spectrum, most notably the fission product fraction that impact the rate and shape of the spectrum. A schema of the detector is presented in figure 2.12a.

#### 2.4.2 OSIRIS

The Online Scintillator Internal Radioactivity Investigation System (OSIRIS) [24] is an ultralow background, 20 m<sup>3</sup> LS detector that will be located in JUNO cavern. It aim to monitor the radioactive contamination, purity and overall response of the LS before it is injected in JUNO. OSIRIS will be located at the end of the purification chain of JUNO, monitoring that the purified LS meet the JUNO requirements. The setup is optimized to detect the fast coincidences decay of <sup>214</sup>Bi – <sup>214</sup>Po and <sup>212</sup>Bi – <sup>212</sup>Po, indicators of the decay chains of U and Th respectively.

##### Detector

OSIRIS is composed of an acrylic vessel that will contains 17t of LS. The LS is instrumented by a PMT array of 64 20 inch PMTs on the top and the side of the vessel. To reach the necessary background level required by the LS purity measurements, in addition to being 700m underground in the experiment cavern, the acrylic vessel is immersed in a tank of ultra pure water. The water is itself instrumented by another array of 20 inch PMTs, acting as muon veto. A schema of the detector is presented in figure 2.12b.

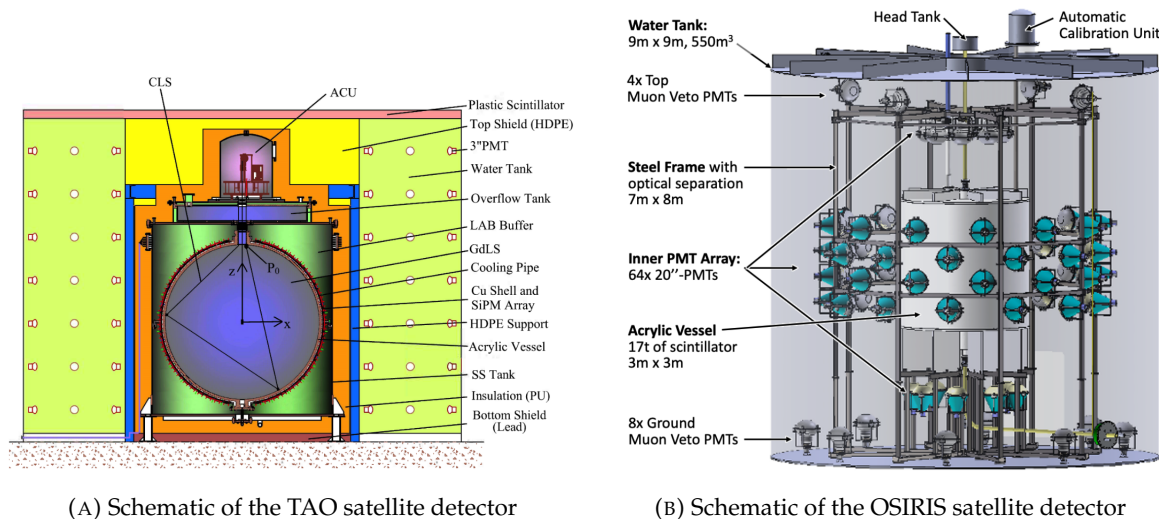


FIGURE 2.12

#### 2.5 Software

The simulation, reconstruction and analysis algorithms are all packaged in the JUNO software, subsequently called the software. It is composed of multiple components integrated in the SNiPER [30] framework:

- Various primary particles simulators for the different kind of events, background and calibration sources.
- A Geant4 [31–33] Monte Carlo (MC) simulation containing the detectors geometries, a custom optical model for the LS and the supporting structures of the detectors. The Geant4 simulation integrate all relevant physics process for JUNO, validated by the collaboration. This step of the simulation is commonly called *Detsim* and compute up to the production of photo-electrons in the PMTs. The optics properties of the different materials and detector components have been measured beforehand to be used to define the material and surfaces in the simulation.

- 430 — An electronic simulation, simulating the response waveform of the PMTs, tracking it through  
431 the digitization process, accounting for effects such as non-linearity, dark noise, Time Transi-  
432 tive Spread (TTS), pre-pulsing, after-pulsing and ringing if the waveform. It's also the step  
433 handling the event triggers and mixing. This step is commonly referenced as *Elecsim*.
- 434 — A waveform reconstruction where the digitized waveform are filtered to remove high-frequency  
435 white noise and then deconvoluted to yield time and charge informations of the photons hits  
436 on the PMTs. This step is commonly referenced as *Calib*.
- 437 — The charge and time informations are used by reconstruction algorithms to reconstruct the  
438 interaction vertex and the deposited energy. This step is commonly reported as *Reco*. See  
439 section 2.6 for more details on the reconstruction.
- 440 — Once the singular events are reconstructed, they go through event pairing and classification  
441 to select IBD events. This step is named Event Classification.
- 442 — The purified signal is then analysed by the analysis framework which depend of the physics  
443 topic of interest.

444 The steps Reco and Event Classification are divided into two category of algorithm. Fast but less  
445 accurate algorithms that are running during the data taking designated as the *Online* algorithms.  
446 Those algorithm are used to take the decision to save the event on tape or to throw it away. More  
447 accurate algorithms that run on batch of events designated *Offline* algorithms. They are used for the  
448 physics analysis. The Offline Reco will be one of the main topic of interest for this thesis.

## 449 2.6 State of the art of the Offline IBD reconstruction in JUNO

450 The main reconstruction method currently run in JUNO is a data-driven method based on a  
451 likelihood maximization [34, 35] using only the LPMTs. The first step is to reconstruct the interaction  
452 vertex from which the energy reconstruction is dependent. It is also necessary for event pairing and  
453 classification.

### 454 2.6.1 Interaction vertex reconstruction

455 To start the likelihood maximization, a rough estimation of the vertex and of the event timing is  
456 needed. We start by estimating the vertex position using a charge based algorithm.

#### 457 Charge based algorithm

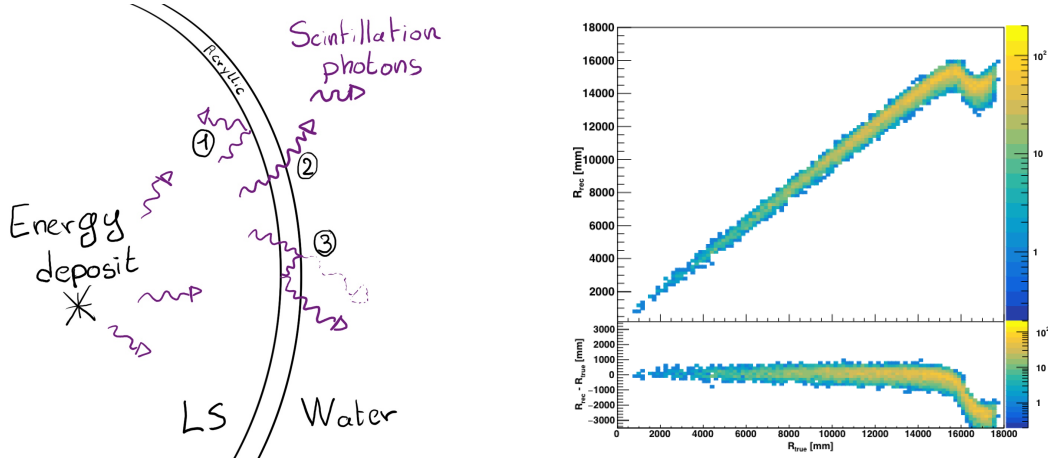
458 The charge-based algorithm is basically base on the charge-weighted average of the PMT position.

$$\vec{r}_{cb} = a \cdot \frac{\sum_i q_i \cdot \vec{r}_i}{\sum_i q_i} \quad (2.3)$$

459 Where  $q_i$  is the reconstructed charge of the pulse of the  $i$ th PMT and  $\vec{r}_i$  is its position.  $\vec{r}_0$  is the  
460 reconstructed interaction position.  $a$  is a scale factor introduced because a weighted average over  
461 a 3D sphere is inherently biased. Using calibration we can estimate  $a \approx 1.3$  [36]. The results in  
462 figure 2.13b shows that the reconstruction is biased from around 15m and further. This is due to the  
463 phenomena called “total reflection area” or TR Area.

464 As depicted in the figure 2.13a the optical photons, given that they have a sufficiently large  
465 incidence angle, can be deviated of their trajectories when passing through the interfaces LS-acrylic  
466 and water-acrylic due to the optical index difference. This cause photons to be lost or to be detected  
467 by PMT further than anticipated if we consider their rectilinear trajectories. This cause the charge  
468 barycenter the be located closer to the center than the event really is.

469 It is to be noted that charge based algorithm, in addition to be biased near the edge of the detector,  
470 does not provide any information about the timing of the event. Therefore, a time based algorithm  
471 needs to be introduced to provide initial values.



(A) Illustration of the different optical photons reflection scenarios. 1 is the reflection of the photon at the interface LS-acrylic or acrylic-water. 2 is the transmission of the photons through the interfaces. 3 is the conduction of the photon in the acrylic.

(B) Heatmap of  $R_{rec}$  and  $R_{rec} - R_{true}$  as a function of  $R_{true}$  for 4MeV prompt signals uniformly distributed in the detector calculated by the charge based algorithm

FIGURE 2.13

#### 472 Time based algorithm

473 The time based algorithm use the distribution of the time of flight corrections  $\Delta t$  (Eq 2.4) of an  
474 event to reconstruct its vertex and  $t_0$ . It follow the following iterations:

- 475 1. Use the charge based algorithm to get an initial vertex to start the iteration.  
476 2. Calculate the time of flight correction for the  $i$ th PMT using

$$\Delta t_i(j) = t_i - \text{tof}_i(j) \quad (2.4)$$

477 where  $j$  is the iteration step,  $t_i$  is the timing of the  $i$ th PMT, and  $\text{tof}_i$  is the time-of-flight of the  
478 photon considering an rectilinear trajectory and an effective velocity in the LS and water (see  
479 [36] for detailed description of this effective velocity). Plot the  $\Delta t$  distribution and label the  
480 peak position as  $\Delta t^{\text{peak}}$  (see fig 2.14a).

- 481 3. Calculate a correction vector  $\vec{\delta}[\vec{r}(j)]$  as

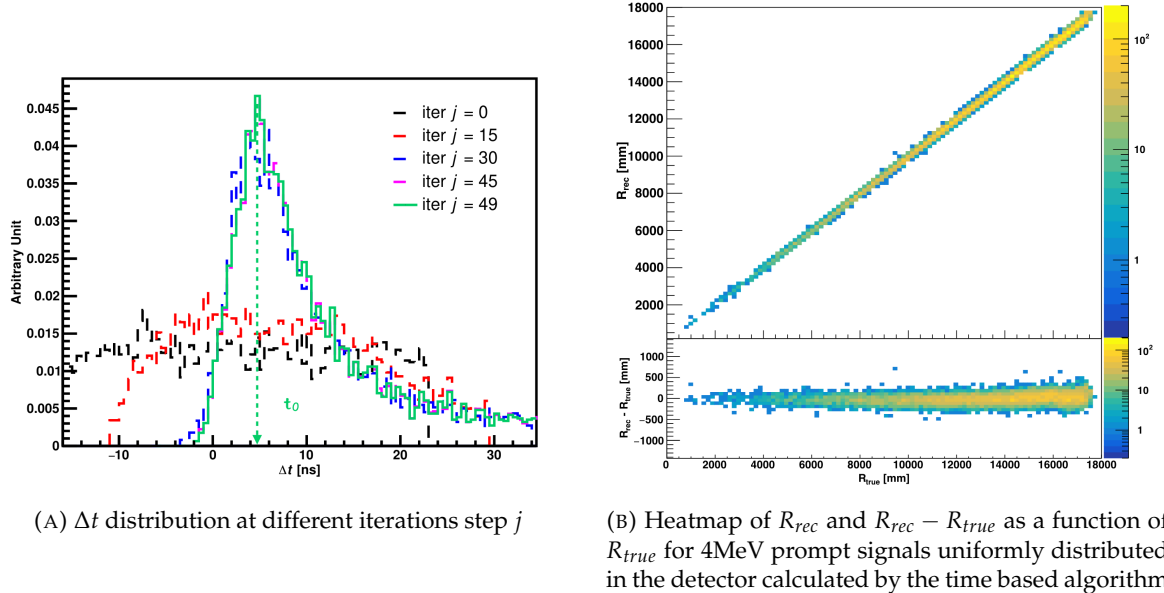
$$\vec{\delta}[\vec{r}(j)] = \frac{\sum_i \left( \frac{\Delta t(j) - \Delta t^{\text{peak}}(j)}{\text{tof}_i(j)} \right) \cdot (\vec{r}_0(j) - \vec{r}_i)}{N^{\text{peak}}(j)} \quad (2.5)$$

482 where  $\vec{r}_0$  is the vertex position at the beginning of this iteration,  $\vec{r}_i$  is the position of the  $i$ th  
483 PMT. To minimize the effect of scattering, dark noise and reflection, only the pulse happening  
484 in a time window (-10 ns, +5 ns) around  $\Delta t^{\text{peak}}$  are considered.  $N^{\text{peak}}$  is the number of PE  
485 collected in this time-window.

- 486 4. if  $|\vec{\delta}[\vec{r}(j)]| < 1\text{mm}$  or  $j \geq 100$ , stop the iteration. Otherwise  $\vec{r}_0(j+1) = \vec{r}_0(j) + \vec{\delta}[\vec{r}(j)]$  and go to  
487 step 2.

488 However because the earliest arrival time is used,  $t_i$  is related to the number photoelectrons  $N_i^{\text{pe}}$   
489 detected by the PMT [37–39]. To reduce bias in the vertex reconstruction, the following equation is  
490 used to correct  $t_i$  into  $t'_i$ :

$$t'_i = t_i - p_0 / \sqrt{N_i^{\text{pe}}} - p_1 - p_2 / N_i^{\text{pe}} \quad (2.6)$$

(A)  $\Delta t$  distribution at different iterations step  $j$ (B) Heatmap of  $R_{rec}$  and  $R_{rec} - R_{true}$  as a function of  $R_{true}$  for 4MeV prompt signals uniformly distributed in the detector calculated by the time based algorithm

491 The parameters  $(p_0, p_1, p_2)$  were optimized to  $(9.42, 0.74, -4.60)$  for Hamamatsu PMTs and  $(41.31,$   
 492  $-12.04, -20.02)$  for NNVT PMTs [36]. The results presented in figure 2.14b shows that the time based  
 493 algorithm provide a more accurate vertex and is unbiased even in the TR area. This results  $(\vec{r}_0, t_0)$  is  
 494 used as initial value for the likelihood algorithm.

#### 495 Time likelihood algorithm

496 The time likelihood algorithm use the residual time expressed as follow

$$t_{\text{res}}^i(\vec{r}_0, t_0) = t_i - \text{tof}_i - t_0 \quad (2.7)$$

497 In a first order approximation, the scintillator time response Probability Density Function (PDF)  
 498 can be described as the emission time profile of the scintillation photons, the Time Transit Spread  
 499 (TTS) and the dark noise of the PMTs. The emission time profile  $f(t_{\text{res}})$  is described like

$$f(t_{\text{res}}) = \sum_k \frac{\rho_k}{\tau_k} e^{-\frac{t_{\text{res}}}{\tau_k}}, \quad \sum_k \rho_k = 1 \quad (2.8)$$

500 as the sum of the  $k$  component that emit light in the LS each one characterised by it's decay time  $\tau_k$   
 501 and intensity fraction  $\rho_k$ . The TTS component is expressed as a gaussian convolution

$$g(t_{\text{res}}) = \frac{1}{\sqrt{2\pi}\sigma} e^{-\frac{(t_{\text{res}}-\nu)^2}{2\sigma^2}} \cdot f(t_{\text{res}}) \quad (2.9)$$

502 where  $\sigma$  is the TTS of PMTs and  $\nu$  is the average transit time. The dark noise is not correlated with any  
 503 physical events and considered as constant rate over the time window considered  $T$ . By normalizing  
 504 the dark noise probability  $\epsilon(t_{\text{res}})$  as  $\int_T \epsilon(t_{\text{res}}) dt_{\text{res}} = \epsilon_{\text{dn}}$ , it can be integrated in the PDF as

$$p(t_{\text{res}}) = (1 - \epsilon_{\text{dn}}) \cdot g(t_{\text{res}}) + \epsilon(t_{\text{res}}) \quad (2.10)$$

505 The distribution of the residual time  $t_{\text{res}}$  of an event can then be compared to  $p(t_{\text{res}})$  and the best

506 fitting vertex  $\vec{r}_0$  and  $t_0$  can be chosen by minimizing

$$\mathcal{L}(\vec{r}_0, t_0) = -\ln \left( \prod_i p(t_{\text{res}}^i) \right) \quad (2.11)$$

507 The parameter of Eq. 2.10 can be measured experimentally. The results shown in figure 2.15  
 508 used PDF from monte carlo simulation. The results shows that  $R_{\text{rec}} - R_{\text{true}}$  is biased depending  
 509 on the energy. While this could be corrected using calibration, another algorithm based on charge  
 510 likelihood was developed to correct this problem.

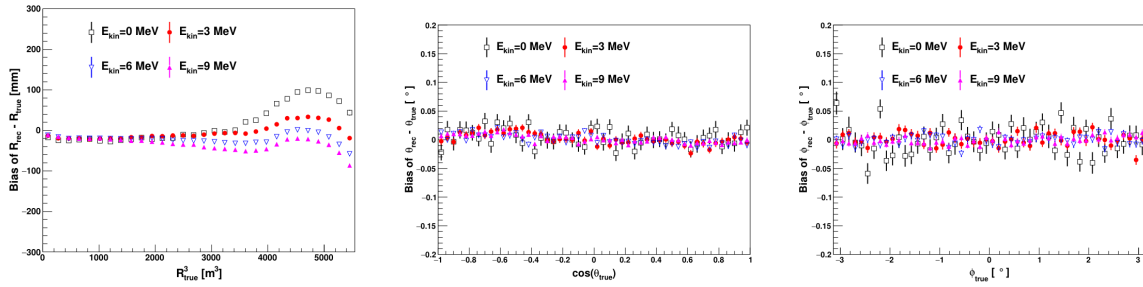


FIGURE 2.15 – Bias of the reconstructed radius  $R$  (left),  $\theta$  (middle) and  $\phi$  (right) for multiple energies by the time likelihood algorithm

### 511 Charge likelihood algorithm

512 Similarly to the time likelihood algorithms that use a timing PDF, the charge likelihood algorithm  
 513 use a PE PDF for each PMT depending on the energy and position of the event. With  $\mu(\vec{r}_0, E)$  the  
 514 mean expected number of PE detected by each PMT, the probability to observe  $N_{pe}$  in a PMT follow  
 515 a Poisson distribution. Thus

- 516 — The probability to observe no hit ( $N_{pe} = 0$ ) in the  $j$ th PMT is  $P_{\text{nohit}}^j(\vec{r}_0, E) = e^{-\mu_j}$
- 517 — The probability to observe  $N_{pe} \neq 0$  in the  $i$ th PMT is  $P_{\text{hit}}^i(\vec{r}_0, E) = \frac{\mu^{N_{pe}^i} e^{-\mu_i}}{N_{pe}^i!}$

518 Therefore, the probability to observe a specific hit pattern can be expressed as

$$P(\vec{r}_0, E) = \prod_j P_{\text{nohit}}^j(\vec{r}_0, E) \cdot \prod_i P_{\text{hit}}^i(\vec{r}_0, E) \quad (2.12)$$

519 The best fit values of  $\vec{R}_0$  and  $E$  can then be calculated by minimizing the negative log-likelihood

$$\mathcal{L}(\vec{r}_0, E) = -\ln(P(\vec{r}_0, E)) \quad (2.13)$$

520 In principle,  $\mu_i(\vec{r}_0, E)$  could be expressed

$$\mu_i(\vec{r}_0, E) = Y \cdot \frac{\Omega(\vec{r}_0, r_i)}{4\pi} \cdot \epsilon_i \cdot f(\theta_i) \cdot e^{-\sum_m \frac{d_m}{\zeta_m}} \cdot E + \delta_i \quad (2.14)$$

521 where  $Y$  is the energy scale factor,  $\Omega(\vec{r}_0, r_i)$  is the solid angle of the  $i$ th PMT,  $\epsilon_i$  is its detection  
 522 efficiency,  $f(\theta_i)$  its angular response,  $\zeta_m$  is the attenuation length in the materials and  $\delta_i$  the expected  
 523 number of dark noise.

524 However Eq. 2.14 assume that the scintillation light yield is linear with energy and describe  
 525 poorly the contribution of indirect light, shadow effect due to the supporting structure and the  
 526 total reflection effects. The solution is to use data driven methods to produce the pdf by using the  
 527 calibrations sources and position described in section 2.3. In the results presented in figures 2.16, the  
 528 PDF was produced using MC simulation and 29 specific calibrations position [36] along the Z-axis

of the detector. We see that the charge likelihood algorithm show little bias in the TR area and a

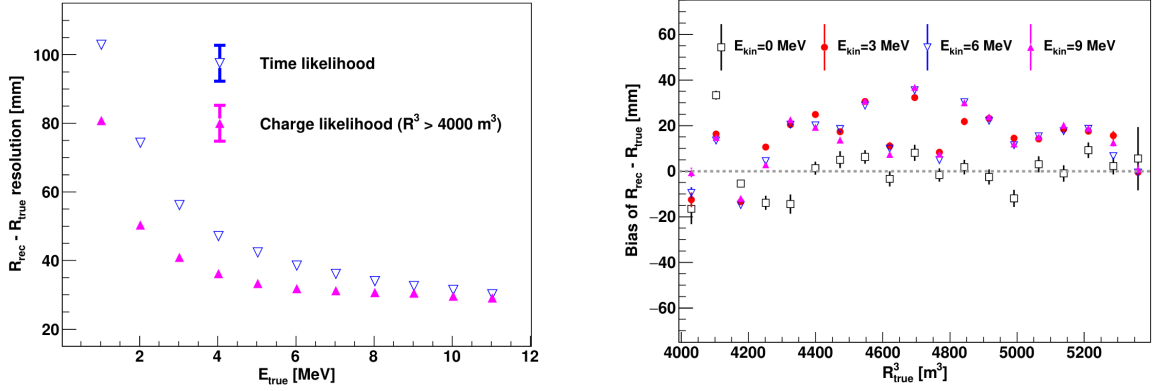


FIGURE 2.16 – On the left: Resolution of the reconstructed  $R$  as a function of the energy in the TR area ( $R^3 > 4000 \text{ m}^3 \equiv R > 16 \text{ m}$ ) by the charge and time likelihood algorithms. On the right: Bias of the reconstructed  $R$  in the TR area for different energies by the charge likelihood algorithm

better resolution than the time likelihood. The figure 2.17 shows the radial resolution of the different algorithm presented for this section, we can see the refinement at each step and that the charge likelihood yield the best results.

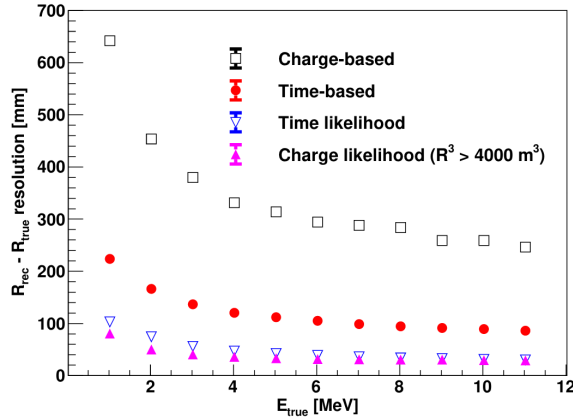


FIGURE 2.17 – Radial resolution of the different vertex reconstruction algorithms as a function of the energy

The charge based likelihood algorithms already give some information on the energy as Eq. 2.13 is minimized but the energy can be further refined as shown in the next section.

## 2.6.2 Energy reconstruction

As explained in section 2.1.1, energy resolution is crucial for the NMO and oscillation parameters measurements. Thus the energy reconstruction algorithm should take into consideration as much detector effect as possible. The following method is a data driven method based on calibration samples inspired by the charge likelihood algorithm described above [40].

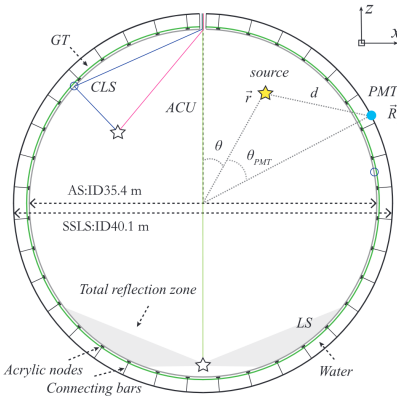


FIGURE 2.18 – Definition of the variables used in the energy reconstruction

### 540 Charge estimation

541 The most important element in the energy reconstruction is  $\mu_i(\vec{r}_0, E)$  described in Eq. 2.14. For  
 542 realistic cases, we also need to take into account the electronics effect that were omitted in the  
 543 previous section. Those effect will cause a charge smearing due to the uncertainties in the  $N_{pe}$   
 544 reconstruction. Thus we define  $\hat{\mu}^L(\vec{r}_0, E)$  which is the expected  $N_{pe}/E$  in the whole detector for an  
 545 event with visible energy  $E_{vis}$  and position  $\vec{r}_0$ . The position of the event and PMTs are now defined  
 546 using  $(r, \theta, \theta_{pmt})$  as defined in figure 2.18.

$$\hat{\mu}(r, \theta, \theta_{pmt}, E_{vis}) = \frac{1}{E_{vis}} \frac{1}{M} \sum_i^M \frac{\bar{q}_i - \mu_i^D}{DE_i}, \quad \mu_i^D = DNR_i \cdot L \quad (2.15)$$

547 where  $i$  runs over the PMTs with the same  $\theta_{pmt}$ ,  $DE_i$  is the detection efficiency of the  $i$ th PMT.  $\mu_i^D$   
 548 is the expected number of dark noise photoelectrons in the time window  $L$ . The time window have  
 549 been optimized to  $L = 280$  ns [40].  $\bar{q}_i$  is the average recorded photoelectrons in the time window  
 550 and  $\bar{Q}_i$  is the expected average charge for 1 photoelectron. The  $N_{pe}$  map is constructed following the  
 551 procedure described in [35].

### 552 Time estimation

553 The second important observable is the hit time of photons that was previously defined in Eq.  
 554 2.7. It is here refined as

$$t_r = t_h - \text{tof} - t_0 = t_{LS} + t_{TT} \quad (2.16)$$

555 where  $t_h$  is the time of hit,  $t_{LS}$  is the scintillation time and  $t_{TT}$  the transit time of PMTs that is described  
 556 by a gaussian

$$t_{TT} = \mathcal{N}(\bar{\mu}_{TT} + t_d, \sigma_{TT}) \quad (2.17)$$

557 where  $\bar{\mu}_{TT}$  is the mean transit time in PMTs,  $\sigma_{TT}$  is the Transit Time Spread (TTS) of the PMTs and  $t_d$   
 558 is the delay time in the electronics. The effective refraction index of the LS is also corrected to take  
 559 into account the propagation distance in the detector.

560 The timing PDF  $P_T(t_r | r, d, \mu_l, \mu_d, k)$  can now be generated using calibration sources [40]. This PDF  
 561 describe the probability that the residual time of the first photon hit is in  $[t_r, t_r + \delta]$  with  $r$  the radius  
 562 of the event vertex,  $d = |\vec{r} - \vec{r}_{PMT}|$  the propagation distance,  $\mu_l$  and  $\mu_d$  the expected number of PE  
 563 and dark noise in the electronic reading window and  $k$  is the detected number of PE.

564 Now let denote  $f(t, r, d)$  the probability density function of "photoelectron hit a time t" for an

565 event happening at  $r$  where the photons traveled the distance  $d$  in the LS

$$F(t, r, d) = \int_t^L f(t', r, d) dt' \quad (2.18)$$

566 Based on the PDF for one photon  $k = 1$ , one can define

$$P_T^l(t|k = n) = I_n^l [f_l(t) F_l^{n-1}(t)] \quad (2.19)$$

567 where the indicator  $l$  means that the photons comes from the LS and  $I_n^l$  a normalisation factor. To this  
568 pdf we add the probability to have photons coming from the dark noise indicated by the indicator  $d$   
569 using

$$f_d(t) = 1/L, F_d(t) = 1 - \frac{t}{L} \quad (2.20)$$

570 and so for the case where only one photon is detected by the PMT ( $k = 1$ )

$$P_T(t|\mu_l, \mu_d, k = 1) = I_1[P(1, \mu_l)P(0, \mu_d)f_l(t) + P(0, \mu_l)P(1, \mu_d)f_d(t)] \quad (2.21)$$

571 where  $P(k_\alpha, \mu_\alpha)$  is the Poisson probability to detect  $k_\alpha$  PE from  $\alpha \in \{l, d\}$  with the condition  $k_l + k_d = k$ .

573 Now that we have the individual timing and charge probability we can construct the charge  
574 likelihood referred as QMLE:

$$\mathcal{L}(q_1, q_2, \dots, q_N | \vec{r}, E_{vis}) = \prod_{j \in \text{unfired}} e^{-\mu_j} \prod_{i \in \text{fired}} \left( \sum_{k=1}^K P_Q(q_i|k) \cdot P(k, \mu_i) \right) \quad (2.22)$$

575 where  $\mu_i = E_{vis}\hat{\mu}_i^L + \mu_i^D$  and  $P(k, \mu_i)$  is the Poisson probability of observing  $k$  PE.  $P_Q(q_i|k)$  is the  
576 charge pdf for  $k$  PE. And we can also construct the time likelihood referred as TMLE:

$$\mathcal{L}(t_{1,r}, t_{2,r}, \dots, t_{N,r} | \vec{r}, t_0) = \prod_{i \in \text{hit}} \frac{\sum_{k=1}^K P_T(t_{i,r}|r, d, \mu_i^l, \mu_i^d, k) \cdot P(k, \mu_i^l + \mu_i^d)}{\sum_{k=1}^K P(k, \mu_i^l + \mu_i^d)} \quad (2.23)$$

577 where  $K$  is cut to 20 PE and hit is the set of hits satisfying  $-100 < t_{i,r} < 500$  ns.

578 Merging those two likelihood give the charge-time likelihood QTMLLE

$$\mathcal{L}(q_1, q_2, \dots, q_N; t_{1,r}, t_{2,r}, \dots, t_{N,r} | \vec{r}, t_0, E_{vis}) = \mathcal{L}(q_1, q_2, \dots, q_N | \vec{r}, E_{vis}) \cdot \mathcal{L}(t_{1,r}, t_{2,r}, \dots, t_{N,r} | \vec{r}, t_0) \quad (2.24)$$

579 The radial and energy resolutions of the different likelihood are presented in figure 2.19 (from  
580 [40]). We can see the improvement of adding the time information to the vertex reconstruction and  
581 that an increase in vertex precision can bring improvement in the energy resolution, especially at low  
582 energies.

583 Data driven methods prove to be performant in the energy and vertex reconstruction given that  
584 we have enough calibrations sources to produce the PDF. In the next section, we'll see another type  
585 of data-driven method based on machine learning.

### 586 2.6.3 Machine learning for reconstruction

587 Machine learning (ML) is family of data-driven algorithms that are inferring behavior and results  
588 from a training dataset. A overview of methods and detailed explanation of the Neural Network  
589 (NN) subfamily can be found in Chapter 3.

590 The power of ML is the ability to model complex response to a specific problem. In JUNO  
591 the reconstruction problematic can be expressed as follow: knowing that each PMT, large or small,  
592 detected a given number of PE  $Q$  at a given time  $t$  and their position is  $x, y, z$  where did the energy

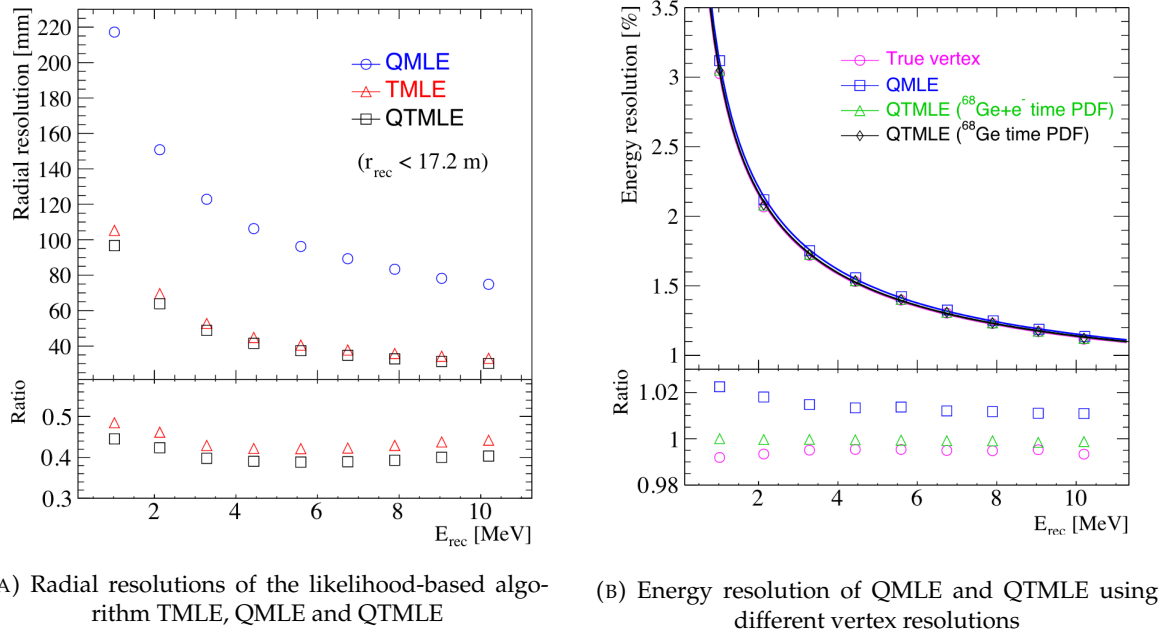


FIGURE 2.19

593 was deposited and how much energy was it, modeling a function that naively goes:

$$\mathbb{R}^{5 \times N_{\text{pmt}}} \mapsto \mathbb{R}^4 \quad (2.25)$$

594 It is worth pointing that while this is already a lot in informations, this is not the rawest representation  
 595 of the experiment. We could indeed replace the charge and time by the waveform in the time  
 596 window of the event but that would lead to an input representation size that would exceed our  
 597 computational limits. Also, due to those computational limits, most of the ML algorithm reduce this  
 598 input phase space either by structurally encoding the information (pictures, graph), by aggregating  
 599 it (mean, variance, ...) or by exploiting invariance and equivariance of the experiment (rotational  
 600 invariance due to the sphericity, ...).

601 For machine learning to converge to performant algorithm, a large dataset exploring all the phase  
 602 space of interest is needed. For the following studies, data from the monte carlo simulation presented  
 603 in section 2.5 are used for training. When the detector will be finished calibrations sources will be  
 604 complementarily be used.

## 605 Boosted Decision Tree (BDT)

606 On of the most classic ML method used in physics in last years is the Boosted Decision Tree (see  
 607 chapter 3.2). They have been explored for vertex reconstruction [41] et for energy reconstruction [41,  
 608 42].

609 For vertex and energy reconstruction a BDT was developed using the aggregated informations  
 610 presented in 2.6.

611 Its reconstruction performances are presented in figure 2.21.

612 A second and more advanced BDT, subsequently named BDTE, that only reconstruct energy use  
 613 a different set of features [42]. They are presented in the table 2.7

Parameter	description
$nHits$	Total number of hits
$x_{cc}, y_{cc}, z_{cc}, R_{cc}$	Coordinates of the center of charge
$ht_{mean}, ht_{std}$	Hit time mean and standard deviation

TABLE 2.6 – Features used by the BDT for vertex reconstruction

AccumCharge	$ht_{5\% - 2\%}$
$R_{cht}$	$pe_{mean}$
$z_{cc}$	$J_{cht}$
$pe_{std}$	$\phi_{cc}$
nPMTs	$ht_{35\% - 30\%}$
$ht_{kurtosis}$	$ht_{20\% - 15\%}$
$ht_{25\% - 20\%}$	$pe_{35\%}$
$R_{cc}$	$ht_{30\% - 25\%}$

TABLE 2.7 – Features used by the BDTE algorithm.  $pe$  and  $ht$  reference the charge and hit-time distribution respectively and the percentages are the quantiles of those distributions.  $cht$  and  $cc$  reference the barycenters of hit time and charge respectively

#### 614 Neural Network (NN)

615 The physics have shown a rising for Neural Network (NN) in the past years for event reconstruction,  
 616 notably in the neutrino community [43–46]. Three type of neural networks have explored for  
 617 event reconstruction in JUNO Deep Neural Network (DNN), Convolutional Neural Network (CNN)  
 618 and Graph Network (GNN). More explanation about those neural network can be found in chapter  
 619 3.

620 The CNN are using 2D projection of the detector representing it as an image with two channel,  
 621 one for the charge  $Q$  and one for the time  $t$ . The position of the PMTs is structurally encoded in the  
 622 pixel containing the information of this PMT. In [41], the pixel is chosen based on a transformation  
 623 of  $\theta$  and  $\phi$  coordinates to the 2D plane and rounded to the nearest pixel. A sufficiently large image  
 624 has been chosen to prevent two PMT to be located in the same pixel. An example of this projection  
 625 can be found in figure 2.20. The performances of the CNN can be found in figure 2.21.

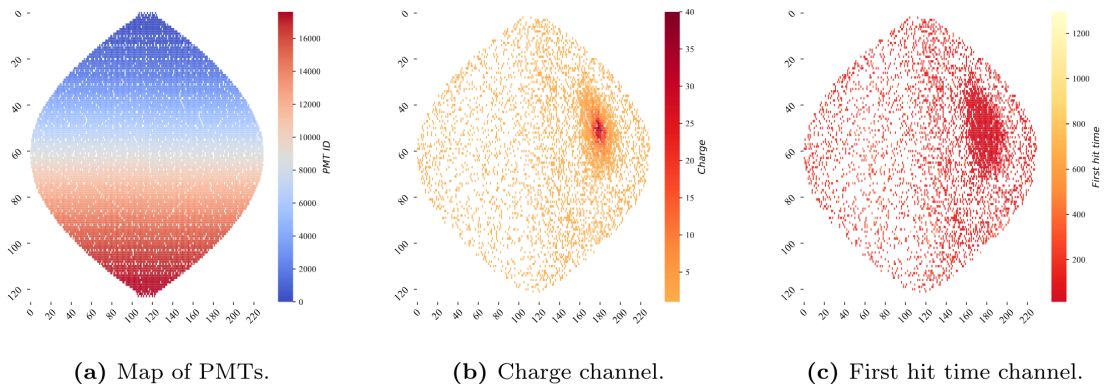


FIGURE 2.20 – Projection of the LPMTs in JUNO on a 2D plane. (a) Show the distribution of all PMTs and (b) and (c) are example of what the charge and time channel looks like respectively

626 Using 2D have the upside of encoding a large part of the informations structurally but loose  
 627 the rotational invariance of the detector. It also give undefined information to the neural network

(what is a pixel without PMT ? What should be its charge and time ?), cause deformation in the representation of the detector (sides of projection) and loose topological informations.

One of the way to present structurally the sphericity of JUNO to a NN is to use a graph: A collection of objects  $V$  called nodes and relations  $E$  called edges, each relation associated to a couple  $v_1, v_2$  forming the graph  $G(E, V)$ . Nodes and edges can hold informations or features. In [41] the nodes, are geometrical region of the detector as defined by the HealPix [47]. The features of the nodes are aggregated informations from the PMTs it contains. The edges contains geographic informations of the nodes relative positions.

This data representation has the advantages to keep the topology of the detector intact. It also permit the use of rotational invariant algorithms for the NN, thus taking advantage of the symmetries of the detector.

The neural network then process the graph using Chebyshev Convolutions [48]. The performances of the GNN are presented in figure 2.21.

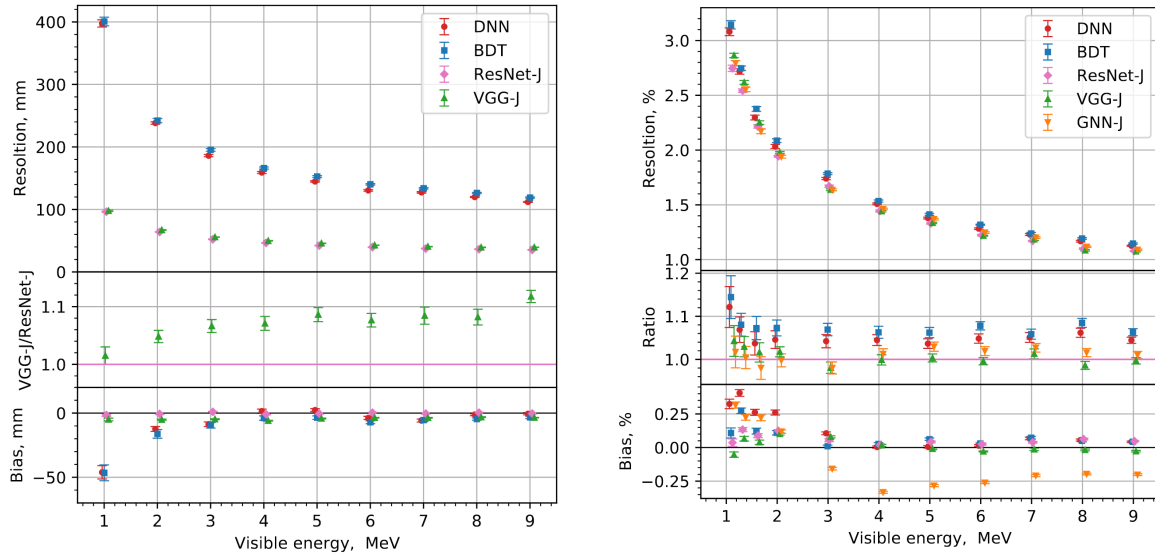


FIGURE 2.21 – Radial (left) and energy (right) resolutions of different ML algorithms.  
The results presented here are from [41]. DNN is a deep neural network, BDT,  
ResNet-J and VGG-J are CNN and GNN-J is a GNN.

Overall ML algorithms show similar performances as classical algorithms in term of energy reconstructions with the more complex structure CNN and GNN showing better performances than BDT and DNN. For vertex reconstruction, the BDT and DNN show poor performance while CNN are on the level of the classical algorithms.

## 2.7 JUNO sensitivity to NMO and precise measurements

Now that the event have been reconstructed, selected and that the non-IBD background have been rejected, we have access to the measured energy flux from JUNO. We consider two spectra, the one measured by the LPMT system and the one measured by the SPMT system. This give rise to three possible analysis: A LPMT only analysis, a SPMT only analysis and a joint analysis. This joint analysis is the subject of the chapter 8 of this thesis.

The following details about JUNO measurement is common to the three analysis. The details and specific of the joint analysis are detailed in chapter 8.

### 653 2.7.1 Theoretical spectrum

654 To extract the oscillation parameters and the NMO from the measured spectrum, it is compared  
 655 to a theoretical spectrum. This theoretical spectrum is produced based on the theory of the three  
 656 flavour oscillation (see section 1.3), the measurements of the calibration and satellite experiments  
 657 and Monte Carlo simulation:

- 658 — The absolute flux and the fission product fraction calibrated by TAO.
- 659 — The estimation of the neutrinos flux from other sources, such as the geoneutrinos, by theoret-  
ical model.
- 660 — The computed cross-section of  $\bar{\nu}_e$  and the LS.
- 661 — The estimation of mislabelled event, such as fast neutron events from cosmic muons, using  
Monte Carlo simulation.
- 662 — The measured bias and resolution of the LPMT and SPMT system by the calibration.
- 663 — The time dependent reactor parameters (age of fuel, instantaneous power of the reactors, etc...)

664 These systematics parameters come with their uncertainties that need to be taken into account by  
 665 the fitting framework. This theoretical spectrum will, in the end, depend of the oscillation parameters  
 666 of interest  $\theta_{13}, \theta_{12}, \Delta m_{21}^2, \Delta m_{31}^2$ . Noise parameters can be included in the parameters spectrum such  
 667 as the earth density  $\rho$  between the power plants and JUNO.

### 670 2.7.2 Fitting procedure

671 The theoretical and measured spectra are represented as two histograms depending on the en-  
 672 ergy. The theoretical spectrum is adjusted with the data using a  $\chi^2$  minimization where  $\chi^2$  is naively  
 673 defined as

$$\chi^2 = \sum_i \frac{(N_{th}^i - N_{data}^i)^2}{\sigma_i^2} \quad (2.26)$$

674 where  $N_{th}^i$  is the number event in the  $i$ th bin of the theoretical spectrum,  $N_{data}^i$  is the number of event  
 675 in the  $i$ th bin of the measured spectrum and  $\sigma_i$  is the uncertainty of this bin. Two classic statistic test  
 676 exist Pearson and Neyman where the difference is the estimation of  $\sigma_i$  parameters.

677 This  $\sigma_i$  is composed of the systematics uncertainties discussed above but also from the statistic  
 678 uncertainty of the spectrum. Considering a Poisson process, the statistic uncertainty is estimated  
 679 as  $\sigma_{stat}^i = \sqrt{N^i}$ . In a Pearson test,  $N^i \equiv N_{th}^i$  whereas in a Neyman test  $N^i \equiv N_{data}^i$ . Under the  
 680 assumption that the content of each bin follow a Gaussian distribution (a Poisson with high enough  
 681 statistic), the two test are equivalent. But studies on Monte Carlo spectrum showed that the Pearson  
 682 and Neyman statistic are biased in opposite direction. It is easily visible where, for the same data,  
 683 Pearson will prefer a higher  $N_{th}^i$  to reduce the ration  $\frac{1}{N_{th}^i}$  whereas Neyman will prefer a lower  $N_{th}^i$  to  
 684 reduce the  $(N_{th}^i - N_{data}^i)$  term.

685 This problematic can be circumvented by summing the two test, yielding the CNP statistic test  
 686 and/or by adding a term

$$\chi^2 = \sum_i \frac{(N_{th}^i - N_{data}^i)^2}{\sigma_i^2} - \ln |\mathbf{V}| \quad (2.27)$$

687 where  $V$  is the covariance matrix of the theoretical spectrum yielding the PearsonV and CNPV  
 688 statistic test.

689 The  $\chi^2$  is minimized by exploring the parameter phase space via gradient descent.

### 690 2.7.3 Physics results

691 The oscillation parameters are directly extracted from the minimization procedure and the error  
 692 can be estimated directly from the procedure. For the NMO, the data are fitted under the two  
 693 assumption of NO and IO. The difference in  $\chi^2$  give us the preferred ordering and the significance  
 694 of our test. Latest studies show that the precision on oscillation parameters after six year of data

- 695 taking will be of 0.2%, 0.3%, 0.5% and 12.1% for  $\Delta m_{31}^2$ ,  $\Delta m_{21}^2$ ,  $\sin^2 \theta_{12}$  and  $\sin^2 \theta_{13}$  respectively [11].  
696 The expected sensitivity to mass ordering is  $3\sigma$  after 6 years [49].

<sub>697</sub> **Chapter 3**

<sub>698</sub> **Machine learning and Artificial  
<sub>699</sub> Neural Network**

<sub>700</sub> **3.1 History of the Machine learning**

<sub>701</sub> **3.2 Boosted Decision Tree (BDT)**

<sub>702</sub> **3.3 Artificial Neural Network (NN)**

<sub>703</sub> **3.3.1 Fully Connected Deep Neural Network (FCDNN)**

<sub>704</sub> **3.3.2 Convolutional Neural Network (CNN)**

<sub>705</sub> **3.3.3 Graph Neural Network (GNN)**

<sub>706</sub> **3.3.4 Adversarial Neural Network (ANN)**

<sub>707</sub> **Generative Adversarial Network (GAN)**

<sub>708</sub> **Reinforcement Learning (RL)**

<sub>709</sub> **Random Search (RS)**

<sub>710</sub> **Bayesian Optimization**



<sup>711</sup> Chapter 4

<sup>712</sup> **Image recognition for IBD  
reconstruction with the SPMT system**

<sup>713</sup> **Image reconstruction for IBD  
reconstruction with the SPMT system**



<sup>714</sup> **Chapter 5**

<sup>715</sup> **Graph representation of JUNO for IBD  
reconstruction with the LPMT system**

<sup>716</sup>



<sup>717</sup> Chapter 6

<sup>718</sup> **Reliability of machine learning  
methods**

<sup>719</sup>



<sup>720</sup> **Chapter 7**

<sup>721</sup> **Discrimination of e+/e- events in  
JUNO**

<sup>722</sup>



<sup>723</sup> **Chapter 8**

<sup>724</sup> **Joint fit between the SPMT and LPMT  
spectra**

<sup>725</sup>



<sup>726</sup> **Chapter 9**

<sup>727</sup> **Conclusion**



# 728 Bibliography

- 729 [1] Liang Zhan, Yifang Wang, Jun Cao, and Liangjian Wen. "Determination of the Neutrino Mass  
 730 Hierarchy at an Intermediate Baseline". *Physical Review D* 78.11 (Dec. 10, 2008), 111103. ISSN:  
 731 1550-7998, 1550-2368. DOI: [10 . 1103 / PhysRevD . 78 . 111103](https://doi.org/10.1103/PhysRevD.78.111103). eprint: [0807 . 3203 \[hep-ex, physics:hep-ph\]](https://arxiv.org/abs/0807.3203). URL: [http://arxiv.org/abs/0807.3203](https://arxiv.org/abs/0807.3203) (visited on 09/18/2023).
- 733 [2] Fengpeng An et al. "Neutrino Physics with JUNO". *Journal of Physics G: Nuclear and Particle  
 734 Physics* 43.3 (Mar. 1, 2016), 030401. ISSN: 0954-3899, 1361-6471. DOI: [10 . 1088 / 0954 - 3899 / 43 / 3 / 030401](https://doi.org/10.1088/0954-3899/43/3/030401). eprint: [1507 . 05613 \[hep-ex, physics:physics\]](https://arxiv.org/abs/1507.05613). URL: [http://arxiv.org/abs/1507.05613](https://arxiv.org/abs/1507.05613) (visited on 07/28/2023).
- 737 [3] Liang Zhan, Yifang Wang, Jun Cao, and Liangjian Wen. "Experimental Requirements to Determine  
 738 the Neutrino Mass Hierarchy Using Reactor Neutrinos". *Physical Review D* 79.7 (Apr. 14,  
 739 2009), 073007. ISSN: 1550-7998, 1550-2368. DOI: [10 . 1103 / PhysRevD . 79 . 073007](https://doi.org/10.1103/PhysRevD.79.073007). eprint: [0901 . 2976 \[hep-ex\]](https://arxiv.org/abs/0901.2976). URL: [http://arxiv.org/abs/0901.2976](https://arxiv.org/abs/0901.2976) (visited on 09/18/2023).
- 741 [4] A. A. Hahn, K. Schreckenbach, W. Gelletly, F. von Feilitzsch, G. Colvin, and B. Krusche. "Antineutrino spectra from 241Pu and 239Pu thermal neutron fission products". *Physics Letters B*  
 742 218.3 (Feb. 23, 1989), 365–368. ISSN: 0370-2693. DOI: [10 . 1016 / 0370 - 2693 \(89\) 91598 - 0](https://doi.org/10.1016/0370-2693(89)91598-0). URL:  
 744 <https://www.sciencedirect.com/science/article/pii/0370269389915980> (visited on  
 745 01/16/2024).
- 746 [5] Th A. Mueller et al. "Improved Predictions of Reactor Antineutrino Spectra". *Physical Review C*  
 747 83.5 (May 23, 2011), 054615. ISSN: 0556-2813, 1089-490X. DOI: [10 . 1103 / PhysRevC . 83 . 054615](https://doi.org/10.1103/PhysRevC.83.054615).  
 748 eprint: [1101 . 2663 \[hep-ex, physics:nucl-ex\]](https://arxiv.org/abs/1101.2663). URL: [http://arxiv.org/abs/1101.2663](https://arxiv.org/abs/1101.2663)  
 749 (visited on 01/16/2024).
- 750 [6] F. von Feilitzsch, A. A. Hahn, and K. Schreckenbach. "Experimental beta-spectra from 239Pu  
 751 and 235U thermal neutron fission products and their correlated antineutrino spectra". *Physics  
 752 Letters B* 118.1 (Dec. 2, 1982), 162–166. ISSN: 0370-2693. DOI: [10 . 1016 / 0370 - 2693 \(82\) 90622 - 0](https://doi.org/10.1016/0370-2693(82)90622-0).  
 753 URL: <https://www.sciencedirect.com/science/article/pii/0370269382906220> (visited  
 754 on 01/16/2024).
- 755 [7] K. Schreckenbach, G. Colvin, W. Gelletly, and F. Von Feilitzsch. "Determination of the antineu-  
 756 trino spectrum from 235U thermal neutron fission products up to 9.5 MeV". *Physics Letters B*  
 757 160.4 (Oct. 10, 1985), 325–330. ISSN: 0370-2693. DOI: [10 . 1016 / 0370 - 2693 \(85\) 91337 - 1](https://doi.org/10.1016/0370-2693(85)91337-1). URL:  
 758 <https://www.sciencedirect.com/science/article/pii/0370269385913371> (visited on  
 759 01/16/2024).
- 760 [8] Patrick Huber. "On the determination of anti-neutrino spectra from nuclear reactors". *Physical  
 761 Review C* 84.2 (Aug. 29, 2011), 024617. ISSN: 0556-2813, 1089-490X. DOI: [10 . 1103 / PhysRevC . 84 . 024617](https://doi.org/10.1103/PhysRevC.84.024617). eprint: [1106 . 0687 \[hep-ex, physics:hep-ph, physics:nucl-ex, physics:nucl-th\]](https://arxiv.org/abs/1106.0687).  
 763 URL: [http://arxiv.org/abs/1106.0687](https://arxiv.org/abs/1106.0687) (visited on 01/16/2024).
- 764 [9] P. Vogel, G. K. Schenter, F. M. Mann, and R. E. Schenter. "Reactor antineutrino spectra and  
 765 their application to antineutrino-induced reactions. II". *Physical Review C* 24.4 (Oct. 1, 1981).  
 766 Publisher: American Physical Society, 1543–1553. DOI: [10 . 1103 / PhysRevC . 24 . 1543](https://doi.org/10.1103/PhysRevC.24.1543). URL:  
 767 <https://link.aps.org/doi/10.1103/PhysRevC.24.1543> (visited on 01/16/2024).

- [10] D. A. Dwyer and T. J. Langford. "Spectral Structure of Electron Antineutrinos from Nuclear Reactors". *Physical Review Letters* 114.1 (Jan. 7, 2015), 012502. ISSN: 0031-9007, 1079-7114. DOI: 10.1103/PhysRevLett.114.012502. eprint: 1407.1281[hep-ex, physics:nucl-ex]. URL: <http://arxiv.org/abs/1407.1281> (visited on 01/16/2024).
- [11] JUNO Collaboration et al. "Sub-percent Precision Measurement of Neutrino Oscillation Parameters with JUNO". *Chinese Physics C* 46.12 (Dec. 1, 2022), 123001. ISSN: 1674-1137, 2058-6132. DOI: 10.1088/1674-1137/ac8bc9. eprint: 2204.13249[hep-ex]. URL: <http://arxiv.org/abs/2204.13249> (visited on 08/11/2023).
- [12] JUNO Collaboration et al. *TAO Conceptual Design Report: A Precision Measurement of the Reactor Antineutrino Spectrum with Sub-percent Energy Resolution*. May 18, 2020. DOI: 10.48550/arXiv.2005.08745. eprint: 2005.08745[hep-ex, physics:nucl-ex, physics:physics]. URL: <http://arxiv.org/abs/2005.08745> (visited on 01/18/2024).
- [13] G. Mention, M. Fechner, Th. Lasserre, Th. A. Mueller, D. Lhuillier, M. Cribier, and A. Letourneau. "Reactor antineutrino anomaly". *Physical Review D* 83.7 (Apr. 29, 2011). Publisher: American Physical Society, 073006. DOI: 10.1103/PhysRevD.83.073006. URL: <https://link.aps.org/doi/10.1103/PhysRevD.83.073006> (visited on 03/05/2024).
- [14] V. Kopeikin, M. Skorokhvatov, and O. Titov. "Reevaluating reactor antineutrino spectra with new measurements of the ratio between  $^{235}\text{U}$  and  $^{239}\text{Pu}$   $\beta^-$  spectra". *Physical Review D* 104.7 (Oct. 25, 2021), L071301. ISSN: 2470-0010, 2470-0029. DOI: 10.1103/PhysRevD.104.L071301. eprint: 2103.01684[hep-ph, physics:nucl-ex, physics:nucl-th]. URL: <http://arxiv.org/abs/2103.01684> (visited on 01/18/2024).
- [15] A. Letourneau et al. "On the origin of the reactor antineutrino anomalies in light of a new summation model with parameterized  $\beta^-$  transitions". *Physical Review Letters* 130.2 (Jan. 10, 2023), 021801. ISSN: 0031-9007, 1079-7114. DOI: 10.1103/PhysRevLett.130.021801. eprint: 2205.14954[hep-ex, physics:hep-ph]. URL: <http://arxiv.org/abs/2205.14954> (visited on 01/16/2024).
- [16] Particle Data Group et al. "Review of Particle Physics". *Progress of Theoretical and Experimental Physics* 2020.8 (Aug. 14, 2020), 083C01. ISSN: 2050-3911. DOI: 10.1093/ptep/ptaa104. URL: <https://doi.org/10.1093/ptep/ptaa104> (visited on 12/04/2023).
- [17] Super-Kamiokande Collaboration et al. "Diffuse Supernova Neutrino Background Search at Super-Kamiokande". *Physical Review D* 104.12 (Dec. 10, 2021), 122002. ISSN: 2470-0010, 2470-0029. DOI: 10.1103/PhysRevD.104.122002. eprint: 2109.11174[astro-ph, physics:hep-ex]. URL: <http://arxiv.org/abs/2109.11174> (visited on 02/28/2024).
- [18] Alessandro Strumia and Francesco Vissani. "Precise quasielastic neutrino/nucleon cross section". *Physics Letters B* 564.1 (July 2003), 42–54. ISSN: 03702693. DOI: 10.1016/S0370-2693(03)00616-6. eprint: astro-ph/0302055. URL: <http://arxiv.org/abs/astro-ph/0302055> (visited on 01/16/2024).
- [19] Daya Bay et al. *Optimization of the JUNO liquid scintillator composition using a Daya Bay antineutrino detector*. July 1, 2020. DOI: 10.48550/arXiv.2007.00314. eprint: 2007.00314[hep-ex, physics:physics]. URL: <http://arxiv.org/abs/2007.00314> (visited on 07/26/2023).
- [20] J. B. Birks. "CHAPTER 3 - THE SCINTILLATION PROCESS IN ORGANIC MATERIALS—I". *The Theory and Practice of Scintillation Counting*. Ed. by J. B. Birks. International Series of Monographs in Electronics and Instrumentation. Jan. 1, 1964, 39–67. ISBN: 978-0-08-010472-0. DOI: 10.1016/B978-0-08-010472-0.50008-2. URL: <https://www.sciencedirect.com/science/article/pii/B9780080104720500082> (visited on 02/07/2024).
- [21] Photomultiplier tube R12860 | Hamamatsu Photonics. URL: [https://www.hamamatsu.com/eu/en/product/optical-sensors/pmt/pmt\\_tube-alone/head-on-type/R12860.html](https://www.hamamatsu.com/eu/en/product/optical-sensors/pmt/pmt_tube-alone/head-on-type/R12860.html) (visited on 02/08/2024).

- 816 [22] Yan Zhang, Ze-Yuan Yu, Xin-Ying Li, Zi-Yan Deng, and Liang-Jian Wen. "A complete optical  
817 model for liquid-scintillator detectors". *Nuclear Instruments and Methods in Physics Research*  
818 *Section A: Accelerators, Spectrometers, Detectors and Associated Equipment* 967 (July 2020), 163860.  
819 ISSN: 01689002. DOI: [10.1016/j.nima.2020.163860](https://doi.org/10.1016/j.nima.2020.163860). eprint: [2003.12212\[physics\]](https://arxiv.org/abs/2003.12212). URL:  
820 <http://arxiv.org/abs/2003.12212> (visited on 02/07/2024).
- 821 [23] Hai-Bo Yang et al. "Light Attenuation Length of High Quality Linear Alkyl Benzene as Liquid  
822 Scintillator Solvent for the JUNO Experiment". *Journal of Instrumentation* 12.11 (Nov. 27, 2017),  
823 T11004–T11004. ISSN: 1748-0221. DOI: [10.1088/1748-0221/12/11/T11004](https://doi.org/10.1088/1748-0221/12/11/T11004). eprint: [1703.01867\[hep-ex, physics:physics\]](https://arxiv.org/abs/1703.01867). URL: <http://arxiv.org/abs/1703.01867> (visited on  
825 07/28/2023).
- 826 [24] JUNO Collaboration et al. *The Design and Sensitivity of JUNO's scintillator radiopurity pre-detector*  
827 OSIRIS. Mar. 31, 2021. DOI: [10.48550/arXiv.2103.16900](https://doi.org/10.48550/arXiv.2103.16900). eprint: [2103.16900\[physics\]](https://arxiv.org/abs/2103.16900). URL:  
828 <http://arxiv.org/abs/2103.16900> (visited on 02/07/2024).
- 829 [25] Angel Abusleme et al. "Mass Testing and Characterization of 20-inch PMTs for JUNO". *The*  
830 *European Physical Journal C* 82.12 (Dec. 24, 2022), 1168. ISSN: 1434-6052. DOI: [10.1140/epjc/s10052-022-11002-8](https://doi.org/10.1140/epjc/s10052-022-11002-8). eprint: [2205.08629\[hep-ex, physics:physics\]](https://arxiv.org/abs/2205.08629). URL: <http://arxiv.org/abs/2205.08629> (visited on 02/08/2024).
- 833 [26] Yang Han. "Dual Calorimetry for High Precision Neutrino Oscillation Measurement at JUNO  
834 Experiment". AstroParticule et Cosmologie, France, Paris U. VII, APC, June 2021.
- 835 [27] R. Acquaferdada et al. "The OPERA experiment in the CERN to Gran Sasso neutrino beam".  
836 *Journal of Instrumentation* 4.4 (Apr. 2009), P04018. ISSN: 1748-0221. DOI: [10.1088/1748-0221/4/04/P04018](https://doi.org/10.1088/1748-0221/4/04/P04018). URL: <https://dx.doi.org/10.1088/1748-0221/4/04/P04018> (visited on  
837 02/29/2024).
- 839 [28] JUNO collaboration et al. "Calibration Strategy of the JUNO Experiment". *Journal of High*  
840 *Energy Physics* 2021.3 (Mar. 2021), 4. ISSN: 1029-8479. DOI: [10.1007/JHEP03\(2021\)004](https://doi.org/10.1007/JHEP03(2021)004). eprint:  
841 [2011.06405\[hep-ex, physics:physics\]](https://arxiv.org/abs/2011.06405). URL: <http://arxiv.org/abs/2011.06405> (visited  
842 on 08/10/2023).
- 843 [29] Hans Th J. Steiger. TAO – *The Taishan Antineutrino Observatory*. Sept. 21, 2022. DOI: [10.48550/arXiv.2209.10387](https://doi.org/10.48550/arXiv.2209.10387). eprint: [2209.10387\[physics\]](https://arxiv.org/abs/2209.10387). URL: <http://arxiv.org/abs/2209.10387>  
844 (visited on 01/16/2024).
- 846 [30] Tao Lin et al. "The Application of SNiPER to the JUNO Simulation". *Journal of Physics: Conference Series* 898.4 (Oct. 2017). Publisher: IOP Publishing, 042029. ISSN: 1742-6596. DOI: [10.1088/1742-6596/898/4/042029](https://doi.org/10.1088/1742-6596/898/4/042029). URL: <https://dx.doi.org/10.1088/1742-6596/898/4/042029>  
847 (visited on 02/27/2024).
- 850 [31] S. Agostinelli et al. "Geant4—a simulation toolkit". *Nuclear Instruments and Methods in Physics*  
851 *Research Section A: Accelerators, Spectrometers, Detectors and Associated Equipment* 506.3 (July 1,  
852 2003), 250–303. ISSN: 0168-9002. DOI: [10.1016/S0168-9002\(03\)01368-8](https://doi.org/10.1016/S0168-9002(03)01368-8). URL: <https://www.sciencedirect.com/science/article/pii/S0168900203013688> (visited on 02/27/2024).
- 854 [32] J. Allison et al. "Geant4 developments and applications". *IEEE Transactions on Nuclear Science*  
855 53.1 (Feb. 2006). Conference Name: IEEE Transactions on Nuclear Science, 270–278. ISSN: 1558-  
856 1578. DOI: [10.1109/TNS.2006.869826](https://doi.org/10.1109/TNS.2006.869826). URL: <https://ieeexplore.ieee.org/document/1610988?isnumber=33833&arnumber=1610988&count=33&index=7> (visited on 02/27/2024).
- 858 [33] J. Allison et al. "Recent developments in Geant4". *Nuclear Instruments and Methods in Physics*  
859 *Research Section A: Accelerators, Spectrometers, Detectors and Associated Equipment* 835 (Nov. 1,  
860 2016), 186–225. ISSN: 0168-9002. DOI: [10.1016/j.nima.2016.06.125](https://doi.org/10.1016/j.nima.2016.06.125). URL: <https://www.sciencedirect.com/science/article/pii/S0168900216306957> (visited on 02/27/2024).

- [34] Wenjie Wu, Miao He, Xiang Zhou, and Haoxue Qiao. "A new method of energy reconstruction for large spherical liquid scintillator detectors". *Journal of Instrumentation* 14.3 (Mar. 8, 2019), P03009–P03009. ISSN: 1748-0221. DOI: [10.1088/1748-0221/14/03/P03009](https://doi.org/10.1088/1748-0221/14/03/P03009). eprint: [1812.01799](https://arxiv.org/abs/1812.01799) [hep-ex, physics:physics]. URL: <http://arxiv.org/abs/1812.01799> (visited on 07/28/2023).
- [35] Guihong Huang et al. "Improving the energy uniformity for large liquid scintillator detectors". *Nuclear Instruments and Methods in Physics Research Section A: Accelerators, Spectrometers, Detectors and Associated Equipment* 1001 (June 11, 2021), 165287. ISSN: 0168-9002. DOI: [10.1016/j.nima.2021.165287](https://doi.org/10.1016/j.nima.2021.165287). URL: <https://www.sciencedirect.com/science/article/pii/S0168900221002710> (visited on 03/01/2024).
- [36] Ziyuan Li et al. "Event vertex and time reconstruction in large volume liquid scintillator detector". *Nuclear Science and Techniques* 32.5 (May 2021), 49. ISSN: 1001-8042, 2210-3147. DOI: [10.1007/s41365-021-00885-z](https://doi.org/10.1007/s41365-021-00885-z). eprint: [2101.08901](https://arxiv.org/abs/2101.08901) [hep-ex, physics:physics]. URL: <http://arxiv.org/abs/2101.08901> (visited on 07/28/2023).
- [37] Gioacchino Ranucci. "An analytical approach to the evaluation of the pulse shape discrimination properties of scintillators". *Nuclear Instruments and Methods in Physics Research Section A: Accelerators, Spectrometers, Detectors and Associated Equipment* 354.2 (Jan. 30, 1995), 389–399. ISSN: 0168-9002. DOI: [10.1016/0168-9002\(94\)00886-8](https://doi.org/10.1016/0168-9002(94)00886-8). URL: <https://www.sciencedirect.com/science/article/pii/0168900294008868> (visited on 03/07/2024).
- [38] C. Galbiati and K. McCarty. "Time and space reconstruction in optical, non-imaging, scintillator-based particle detectors". *Nuclear Instruments and Methods in Physics Research Section A: Accelerators, Spectrometers, Detectors and Associated Equipment* 568.2 (Dec. 1, 2006), 700–709. ISSN: 0168-9002. DOI: [10.1016/j.nima.2006.07.058](https://doi.org/10.1016/j.nima.2006.07.058). URL: <https://www.sciencedirect.com/science/article/pii/S0168900206013519> (visited on 03/07/2024).
- [39] M. Moszyński and B. Bengtson. "Status of timing with plastic scintillation detectors". *Nuclear Instruments and Methods* 158 (Jan. 1, 1979), 1–31. ISSN: 0029-554X. DOI: [10.1016/S0029-554X\(79\)90170-8](https://doi.org/10.1016/S0029-554X(79)90170-8). URL: <https://www.sciencedirect.com/science/article/pii/S0029554X79901708> (visited on 03/07/2024).
- [40] Gui-Hong Huang, Wei Jiang, Liang-Jian Wen, Yi-Fang Wang, and Wu-Ming Luo. "Data-driven simultaneous vertex and energy reconstruction for large liquid scintillator detectors". *Nuclear Science and Techniques* 34.6 (June 17, 2023), 83. ISSN: 2210-3147. DOI: [10.1007/s41365-023-01240-0](https://doi.org/10.1007/s41365-023-01240-0). URL: <https://doi.org/10.1007/s41365-023-01240-0> (visited on 08/17/2023).
- [41] Zhen Qian et al. "Vertex and Energy Reconstruction in JUNO with Machine Learning Methods". *Nuclear Instruments and Methods in Physics Research Section A: Accelerators, Spectrometers, Detectors and Associated Equipment* 1010 (Sept. 2021), 165527. ISSN: 01689002. DOI: [10.1016/j.nima.2021.165527](https://doi.org/10.1016/j.nima.2021.165527). eprint: [2101.04839](https://arxiv.org/abs/2101.04839) [hep-ex, physics:physics]. URL: <http://arxiv.org/abs/2101.04839> (visited on 07/24/2023).
- [42] Arsenii Gavrikov, Yury Malyshkin, and Fedor Ratnikov. "Energy reconstruction for large liquid scintillator detectors with machine learning techniques: aggregated features approach". *The European Physical Journal C* 82.11 (Nov. 14, 2022), 1021. ISSN: 1434-6052. DOI: [10.1140/epjc/s10052-022-11004-6](https://doi.org/10.1140/epjc/s10052-022-11004-6). eprint: [2206.09040](https://arxiv.org/abs/2206.09040) [physics]. URL: <http://arxiv.org/abs/2206.09040> (visited on 07/24/2023).
- [43] R. Abbasi et al. "Graph Neural Networks for low-energy event classification & reconstruction in IceCube". *Journal of Instrumentation* 17.11 (Nov. 2022). Publisher: IOP Publishing, P11003. ISSN: 1748-0221. DOI: [10.1088/1748-0221/17/11/P11003](https://doi.org/10.1088/1748-0221/17/11/P11003). URL: <https://dx.doi.org/10.1088/1748-0221/17/11/P11003> (visited on 04/04/2024).
- [44] S. Reck, D. Guderian, G. Vermariën, A. Domi, and on behalf of the KM3NeT collaboration on behalf of the. "Graph neural networks for reconstruction and classification in KM3NeT". *Journal of Instrumentation* 16.10 (Oct. 2021). Publisher: IOP Publishing, C10011. ISSN: 1748-0221. DOI: [10.1088/1748-0221/16/10/C10011](https://doi.org/10.1088/1748-0221/16/10/C10011). URL: <https://dx.doi.org/10.1088/1748-0221/16/10/C10011> (visited on 04/04/2024).

- [45] The IceCube collaboration et al. “A convolutional neural network based cascade reconstruction for the IceCube Neutrino Observatory”. *Journal of Instrumentation* 16.7 (July 2021). Publisher: IOP Publishing, P07041. ISSN: 1748-0221. DOI: [10.1088/1748-0221/16/07/P07041](https://doi.org/10.1088/1748-0221/16/07/P07041). URL: <https://dx.doi.org/10.1088/1748-0221/16/07/P07041> (visited on 04/04/2024).
- [46] DUNE Collaboration et al. “Neutrino interaction classification with a convolutional neural network in the DUNE far detector”. *Physical Review D* 102.9 (Nov. 9, 2020). Publisher: American Physical Society, 092003. DOI: [10.1103/PhysRevD.102.092003](https://doi.org/10.1103/PhysRevD.102.092003). URL: <https://link.aps.org/doi/10.1103/PhysRevD.102.092003> (visited on 04/04/2024).
- [47] K. M. Górski, E. Hivon, A. J. Banday, B. D. Wandelt, F. K. Hansen, M. Reinecke, and M. Bartelmann. “HEALPix: A Framework for High-Resolution Discretization and Fast Analysis of Data Distributed on the Sphere”. *The Astrophysical Journal* 622 (Apr. 1, 2005). ADS Bibcode: 2005ApJ...622..759G, 759–771. ISSN: 0004-637X. DOI: [10.1086/427976](https://doi.org/10.1086/427976). URL: <https://ui.adsabs.harvard.edu/abs/2005ApJ...622..759G> (visited on 04/04/2024).
- [48] Michaël Defferrard, Xavier Bresson, and Pierre Vandergheynst. *Convolutional Neural Networks on Graphs with Fast Localized Spectral Filtering*. Feb. 5, 2017. DOI: [10.48550/arXiv.1606.09375](https://doi.org/10.48550/arXiv.1606.09375). eprint: [1606.09375\[cs, stat\]](https://arxiv.org/abs/1606.09375). URL: [http://arxiv.org/abs/1606.09375](https://arxiv.org/abs/1606.09375) (visited on 04/04/2024).
- [49] JUNO Collaboration et al. “JUNO Physics and Detector”. *Progress in Particle and Nuclear Physics* 123 (Mar. 2022), 103927. ISSN: 01466410. DOI: [10.1016/j.ppnp.2021.103927](https://doi.org/10.1016/j.ppnp.2021.103927). eprint: [2104.02565\[hep-ex\]](https://arxiv.org/abs/2104.02565). URL: [http://arxiv.org/abs/2104.02565](https://arxiv.org/abs/2104.02565) (visited on 09/18/2023).